AN X-RAY STUDY OF G272.2-3.2 – A NEWLY DISCOVERED SUPERNOVA REMNANT & MSH 11-62 AND 3C58

NASA Grant NAG5-2638

Final Report

For the Period 1 July 1994 through 30 September 2000

Principal Investigator
Dr. Patrick O. Slane

December 2000

Prepared for:

National Aeronautics and Space Administration
Goddard Space Flight Center
Greenbelt, Maryland 20771

Smithsonian Institution
Astrophysical Observatory
Cambridge, Massachusetts 02138

The Smithsonian Astrophysical Observatory
is a member of the
Harvard-Smithsonian Center for Astrophysics

The NASA Technical Officer for this grant is Dr. Nicholas White, Code 668, Laboratory for High Energy Astrophysics, NASA/Goddard Space Flight Center, Greenbelt, Maryland 20771.

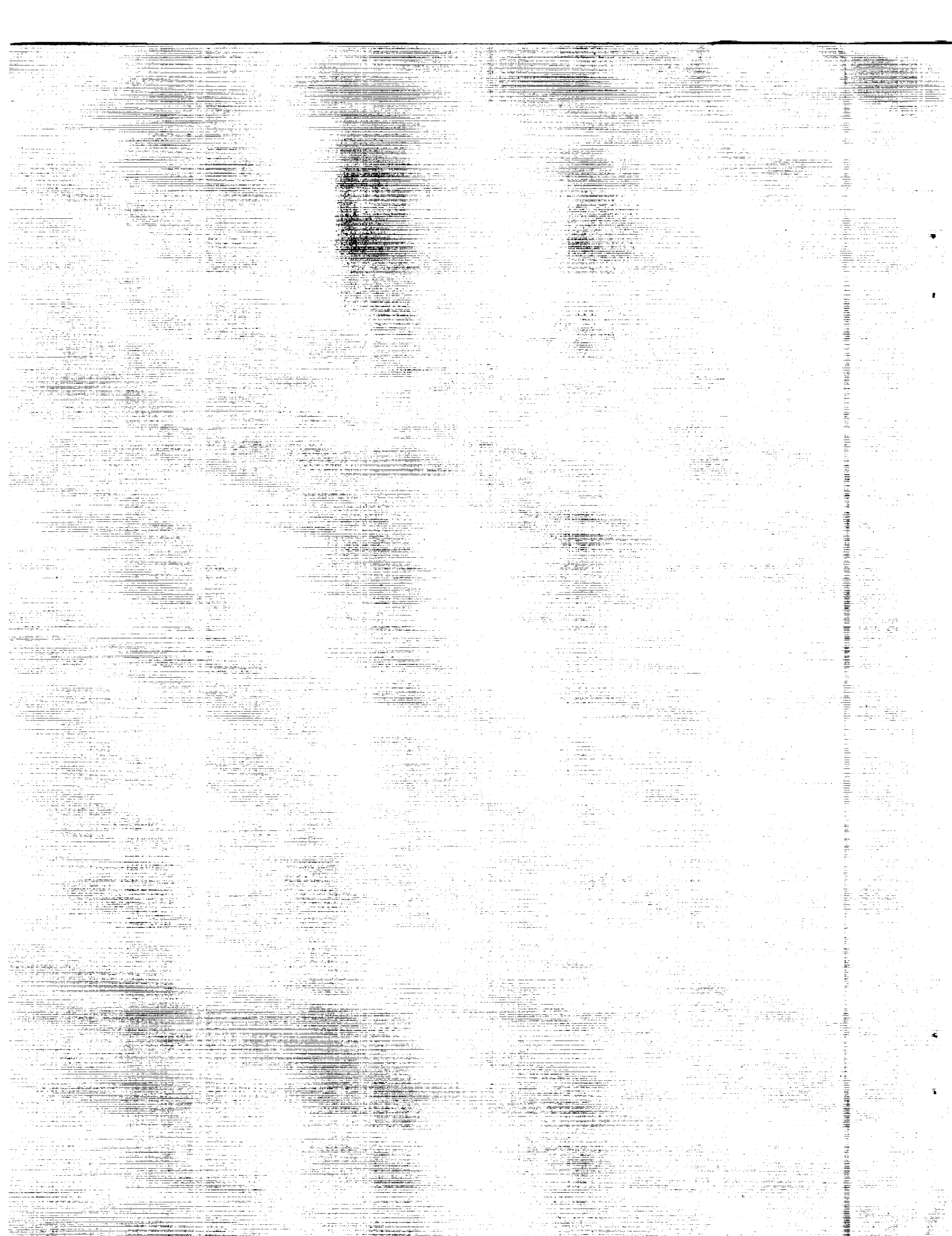

The subject grant is for work on a study of X-ray emission from galactic supernova remnants (SNRs). The purpose of the study is to 1)determine whether the emission from the remnants is thermal or nonthermal; 2)compare the observed temperature and morphological characteristics with models for SNR evolution; and 3)search for any evidence of pulsars associated with the SNRs. We obtained ASCA observations of the remnants MSH 11-61A, W28, CTA 1, 3C58, and G272.2–3.2. Analyses of these data are in various stages of completion as described below.

The ASCA observation of CTA 1 covering the central regions of this remnant has been analyzed. We find that the central spectrum is clearly nonthermal, suggesting the presence of a central pulsar. Properties of a faint central point source observed with ROSAT are consistent with those expected for the pulsar. The results have been summarized in a paper entitled "Nonthermal X-ray Emission from CTA 1" (Slane et al. 1997, ApJ, 485, 221); a reprint of the paper is attached.

The analysis of the 3C58 data is complete, and results were reported in a paper entitled "ASCA Observation of the Crab-like Supernova Remnant 3C58" (Torii, Slane, Kinugasa, Hashimotodani, & Tsunemi 2000, PASJ, 52, No. 5, 87). A reprint of the paper is attached.

Work has been completed on the analysis of data from G272.2–3.2. A paper entitled "New ASCA and ROSAT Study of the Supernova Remnant: G272.2-3.2" (I. M. Harrus, P. Slane, R. Smith, & J. P. Hughes) has been submitted for publication. A preprint of this paper is attached.

Spectra from MSH 11-61A and W28 reveal that the emission is clearly thermal in nature for both sources. Comparisons of the spectral and morphological characteristics with models for SNR evolution in a cloudy interstellar medium (ISM) and for models of radiative-phase remnants are in progress. A paper summarizing the results for MSH 11-61A is currently being circulated among co-authors, and will be submitted for publication in ApJ.

THE ASTROPHYSICAL JOURNAL, 485:221–227, 1997 August 10

NONTHERMAL X-RAY EMISSION FROM CTA 1

PATRICK SLANE,[1] FREDERICK D. SEWARD,[1] RINO BANDIERA,[2] KEN'ICHI TORII,[3] AND HIROSHI TSUNEMI[3,4]
Received 1996 December 19; accepted 1997 March 3

ABSTRACT

CTA 1 is a center-filled supernova remnant (SNR) whose morphology and spectrum indicate the presence of a central pulsar, a synchrotron nebula, and a thermal component associated with the expansion of the blast wave into the interstellar medium. The centrally bright emission surrounds the position of a faint point source of X-rays observed with the *ROSAT* PSPC. Here we report on *ASCA* observations that confirm the nonthermal nature of the diffuse emission from the central regions of the remnant. We also present evidence for weak thermal emission that appears to increase in strength toward the outer boundary of the SNR. Thus, CTA 1 appears to be an X-ray composite remnant. Both the aftermath of the explosive supernova event and the energetic compact core are observable.

Subject headings: ISM: individual (CTA 1) — supernova remnants — X-rays: ISM

1. INTRODUCTION

An important class of supernova remnants (SNRs) is characterized by centrally bright X-ray emission accompanied by a radio shell. In several cases (e.g., W49B [Smith et al. 1985]; W44 [Rho et al. 1994; Harrus et al. 1997]) the X-ray emission is clearly thermal in nature. Our *ROSAT* studies of CTA 1 (Seward, Schmidt, & Slane 1995, hereafter SSS95) suggest a different scenario for this remnant. The central emission is dominated by a power-law component, probably driven by an as yet undiscovered pulsar, while the outer regions are dominated by a thermal component associated with the SNR blast wave. In this paper we present results from new X-ray observations of CTA 1, carried out with the *Advanced Satellite for Cosmology and Astrophysics* (*ASCA*) observatory, that confirm the nonthermal nature of the central emission as well as the presence of a weak soft component which we attribute to thermal emission from the shock-heated swept-up interstellar medium (ISM).

Our initial studies of CTA 1 (SSS95) incorporated three ~10 ks Position Sensitive Proportional Counter (PSPC) observations to map the ~100′ remnant (Fig. 1). A 3 ks HRI observation was used to determine an accurate position for the brightest source in the remnant image (1E 0000+726 which has been subtracted from Fig. 1). Optical observations identified the source as a background active galactic nucleus (AGN); the position of this source is indicated in Figure 1.

The spatial distribution of the X-ray emission, which peaks in the central regions, extends out to the radio shell (Fig. 2); the X-ray rim is sharpest in the south, where the radio shell is brightest (Pineault et al. 1993). A faint point source ($R_{PSPC} = 4.5 \times 10^{-3}$ counts s^{-1}) resides within the bright central region, where the count rate is 0.32 counts s^{-1} averaged over a circle of 10′ radius. A ridge of radio emission extends from the south toward the center of the remnant, but there is no clear evidence of a radio plerion at the position of the X-ray central source. The southern boundary of the X-ray emission coincides with the bright radio shell, and a ridge of emission similar to that seen in the radio image extends back to the bright center. The X-ray emission extends beyond the radio in the northern portions of CTA 1 where the radio shell is incomplete, perhaps suggestive of a blowout into a preexisting cavity (Pineault et al. 1993); recent radio images at higher sensitivity (Pineault et al. 1997) reveal faint radio emission from this region of extended X-ray emission as well.

Spectral studies with the PSPC show clearly that a simple one-temperature thermal spectrum (Raymond & Smith 1977) is not compatible with the data—a result which is not surprising for emission from an SNR. Addition of a power-law component provides an acceptable fit to the data, as does addition of a second, higher temperature, thermal component. The PSPC data cannot discriminate between the two models. However, based upon modeling efforts in which we attempted to reproduce the centrally bright morphology of the remnant (SSS95), we concluded that the temperature profile implied by the thermal model was difficult to reproduce. A plausible alternative interpretation was that CTA 1 is described by a central power law (probably associated with a pulsar) combined with a thermal component which we attribute to the SNR shock.

Spectra extracted from several discrete regions of the remnant show that the power-law component becomes weaker farther from the center of the remnant, consistent with the interpretation of a central plerion (Fig. 3); the power-law component comprises ~90% of the 0.1–2.4 keV flux in the central regions, while the outer regions are dominated by a ~50%–80% thermal component. The PSPC data show some evidence of a softening of the power-law spectrum with radius as well. *ASCA* studies of the Crab-like remnant 3C 58 reveal similar results (Torii et al. 1996).

2. *ASCA* OBSERVATION

The central region of CTA 1 was observed with *ASCA* for 40 ks on 1996 January 25. To increase the available time resolution for the GIS data, some telemetry bits from the pulse-height analyzer (PHA) and rise-time data were sacrificed. The resulting 256 PHA channels do not degrade the spectral resolution beyond that inherent to the GIS. However, all rise-time information was sacrificed for data taken with medium bit rate. Such loss of rise-time data does

[1] Harvard-Smithsonian Center for Astrophysics, 60 Garden Street, Cambridge, MA 02138.
[2] Osservatorio Astrofisico di Arcetri, Largo E Fermi 5, 50125 Firenze, Italy.
[3] Department of Earth and Space Science, Osaka University 1-1, Machikaneyama-cho, Toyonaka, Osaka, 560, Japan.
[4] CREST, Japan Science and Technology Corporation (JST).

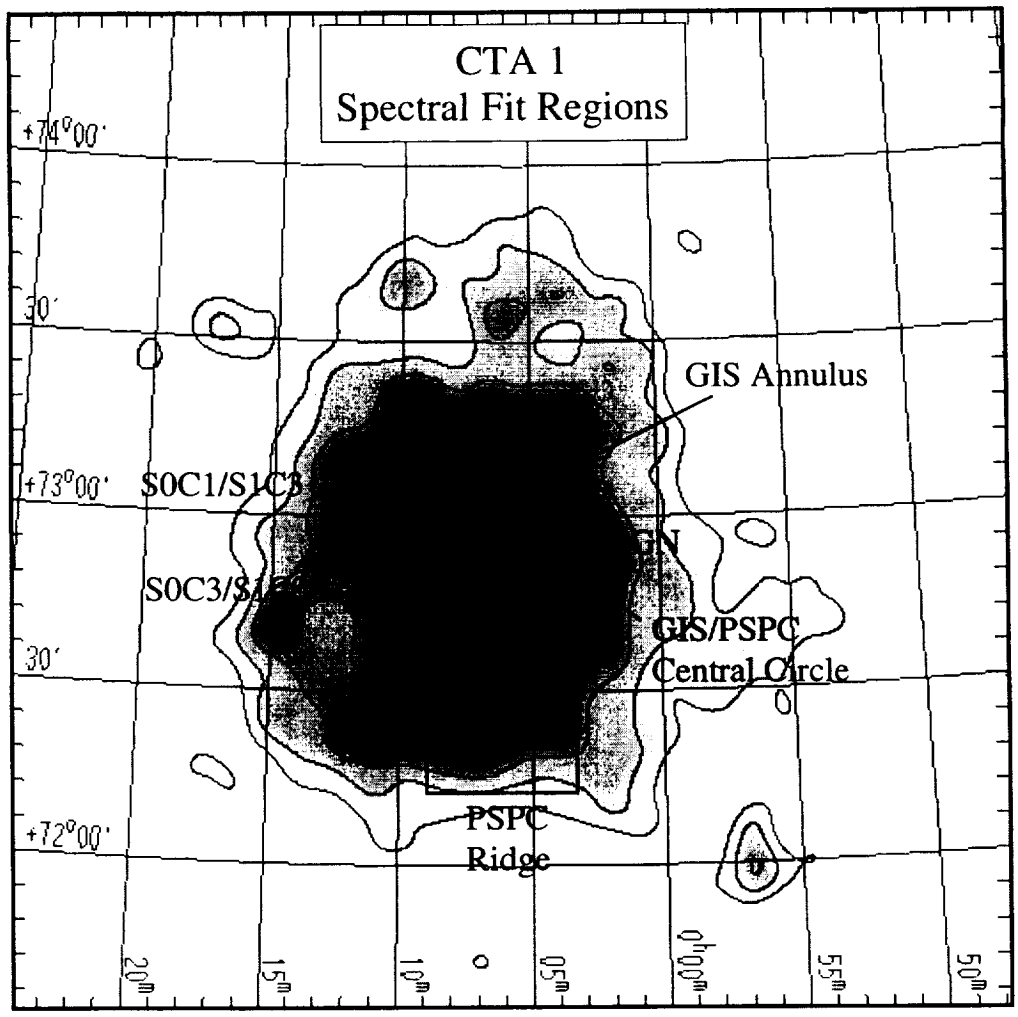

FIG. 1.—PSPC image of CTA 1. Spectral results are consistent with a power law that is strongest at the bright central region, in combination with a soft thermal component that may be associated with shocked ISM. The grid is in J2000 coordinates. Spectral fitting fields are indicated schematically: the inner circle corresponds to central GIS and PSPC fields; the outer annulus corresponds to the outer GIS field; SIS fields are as indicated; PSPC ridge refers to one discrete region used in SSS95 and illustrated in Fig. 3. The location of the AGN which has been subtracted from image is indicated with a plus sign.

slightly compromise the ability to reject background, but the resulting effect on spectral characterization is not large. The approach then provides time resolution of ~4 ms for medium bit rate telemetry data and ~15 ms for high bit rate data. This resolution is crucial to a search for high-frequency pulsations which might arise from a central pulsar.

After screening to remove data taken at low magnetic rigidity or small Earth angle, we obtained a total of ~20,000 events (~41 ks) from each GIS detector (~57% of which was in high bit rate mode). The SIS data were acquired in 2 CCD mode because of the reduced spectral resolution and increased problems with flickering pixels associated with 4 CCD mode. Chips S0C1 and S1C3 covered the region centered on the peak X-ray brightness, while chips S0C3 and S1C1 covered the region directly south of the center (Fig. 1). After screening and removal of flickering pixels, we obtained a total of ~12,000 events from each SIS detector (approximately 7500 of which were from the chip covering the bright central region).

3. ANALYSIS

3.1. *Spectral*

Our investigation included separate analysis of the GIS and SIS data as well as joint fits using the GIS, SIS, and PSPC data. Background for the *ASCA* data was obtained from blank-sky observations available in the *ASCA* data archive. While these were carried out at high Galactic latitude, they provide an adequate description of the background for CTA 1, which has a Galactic latitude of 10°.5; the background-subtracted spectra show no signs of a hard thermal component with line features which might be expected from Galactic ridge emission at lower latitudes (Yamauchi et al. 1996). The GIS and SIS data both reveal featureless spectra consistent with a power law of photon index $\alpha \sim 2$. In each case, addition of a small thermal component at $kT \sim 0.2$ keV yields a statistically significant improvement in the fit.

For more detailed analysis, we extracted GIS2, GIS3, and PSPC spectra from circular regions of radius 9'.2 centered

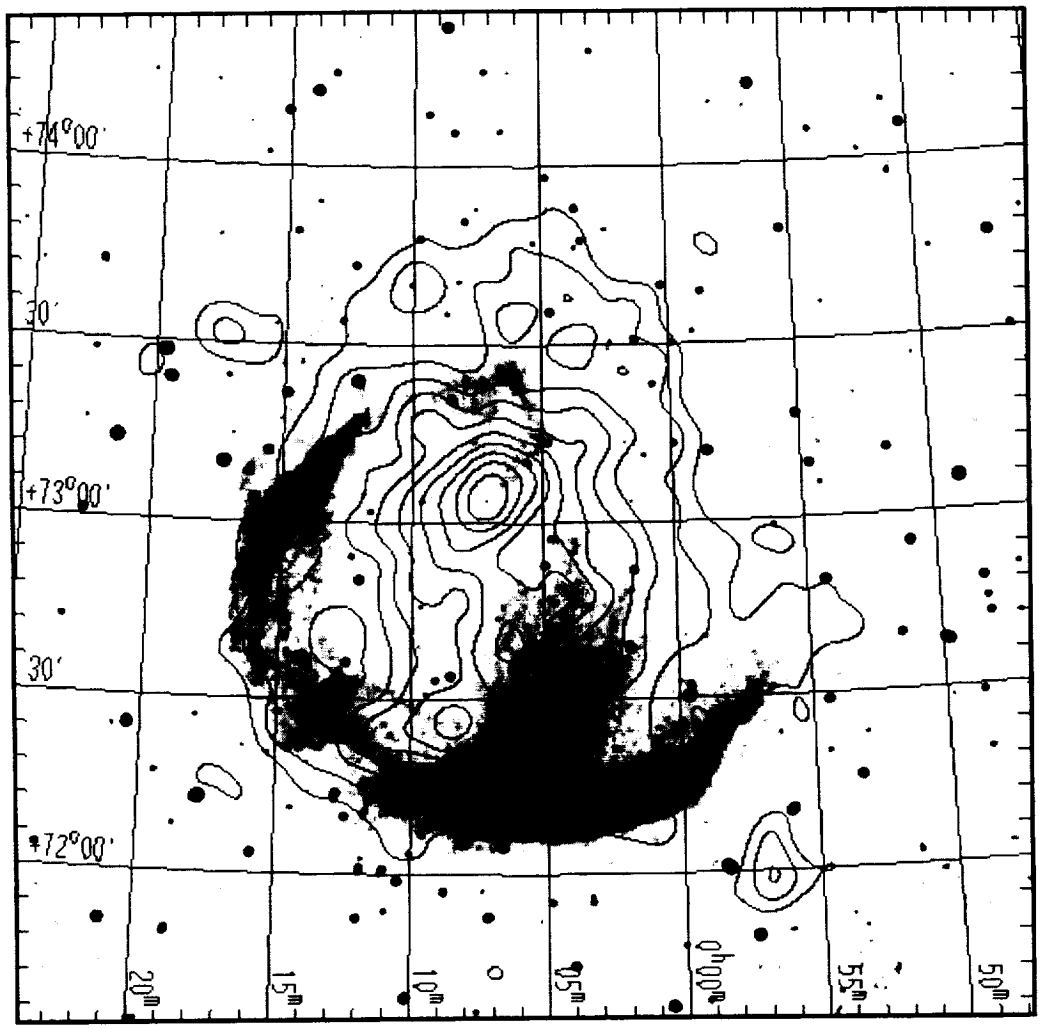

FIG. 2.—Continuum emission from CTA 1 at 1420 MHz (Pineault et al. 1993). X-ray contours correspond to the *ROSAT* PSPC image. The southern edge of the X-ray emission corresponds well with the bright radio shell. Similarly, there is evidence in the radio for a bridgelike structure extending toward the center, similar to that seen in X-rays. The most recent radio maps (Pineault et al. 1996) show faint radio emission extending to the outer X-ray contours in the north and northwest.

on the bright central region. We performed joint fits on these data along with SIS data from chips S0C1 and S1C3. The inclusion of the PSPC data was particularly important in helping to constrain the value of N_H. Normalizations for each detector were varied independently to allow for differences in field of view and point-spread function. The fit to a composite thermal/nonthermal spectrum yields a reduced χ^2 of 1.17 for the best-fit parameters given in Table 1.

We next searched for evidence of spectral variations across the remnant. Here we fixed the column density at the best-fit value derived above. Using the SIS chip centered on the bright central region, the measured photon index is $\alpha = 2.1 \pm 0.1$ (Fig. 4), the same within the small uncertainty as that for the Crab Nebula. The power-law fit is sta-

TABLE 1

CTA 1 SPECTRAL PARAMETERS

Region	Data	Parameter	Value
Central 9'.2	GIS, SIS, and PSPC	N_H	$2.8^{+0.6}_{-0.5} \times 10^{21}$ cm^{-2}
Central 9'.2	GIS, SIS, and PSPC	α (photon)	$2.03^{+0.05}_{-0.07}$
Central 9'.2	GIS, SIS, and PSPC	kT	0.21 ± 0.03 keV
$0 < R < 9'.2$	GIS	F_X (thermal)	2.7×10^{-12} ergs cm^{-2} s^{-1}
$0 < R < 9'.2$	GIS	F_X (nonthermal)	9.5×10^{-12} ergs cm^{-2} s^{-1}
$9'.2 < R < 18'.5$	GIS	F_X (thermal)	1.3×10^{-11} ergs cm^{-2} s^{-1}
$9'.2 < R < 18'.5$	GIS	F_X (nonthermal)	1.4×10^{-11} ergs cm^{-2} s^{-1}

NOTE.—All fluxes are 0.5–10 keV.

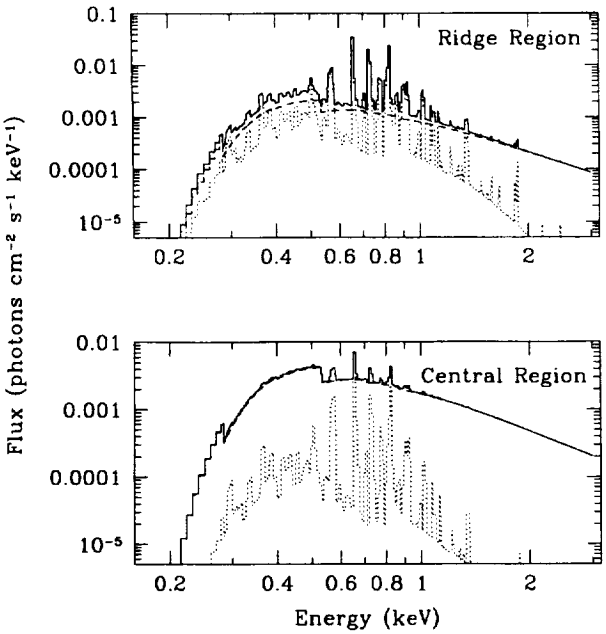

FIG. 3.—Best-fit spectral components and their sum for power-law plus thermal model to PSPC data extracted from a circular central region (*lower panel*) and a rectangular region along the southern ridge of CTA 1 (see Fig. 1). The power-law component is dominant in the central region, while the thermal component comprises 50% of the flux in the ridge region. Similar results are observed from *ASCA* data, although only the central region was mapped (see text).

tistically improved with the addition of a soft thermal component ($kT = 0.21 \pm 0.03$ keV), which contributes $\sim 25\%$ of the unabsorbed 0.5–10 keV flux ($\sim 10\%$ of the observed flux). The spectrum from the chip placed directly south of the bright center is similar to the above, but the thermal component is stronger ($\sim 40\%$ of the unabsorbed flux). The power-law index is 2.3 ± 0.1, suggesting a softening of the emission with increasing radius.

Dividing the GIS spectra into two regions—a central circle of radius 9′.2 and a surrounding annulus of thickness 9′.2—confirms the expected increase in the contribution of the thermal component at larger radii by a factor of ~ 2. The relative flux values for these regions, assuming the best-fit spectral values described above, are listed in Table 1.

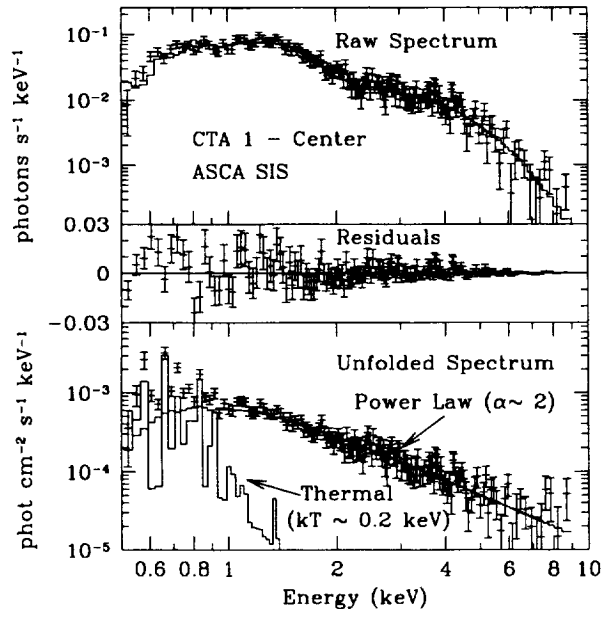

FIG. 4.—*ASCA* data extracted from a SIS chip centered on the central region of CTA 1 (see Fig. 1). *Upper panel*: Raw spectrum with best-fit power-law plus thermal model. *Middle panel*: Residuals between data and best-fit model. *Lower panel*: Unfolded spectrum and model components. Compare with predictions based upon PSPC spectra (Fig. 2—note that PSPC central spectral region does not cover the same angular size as the SIS chip).

3.2. *Timing*

A search for pulsations associated with a central pulsar was carried out using the GIS data. Using both high and medium bit rate data, we extracted all events from a circle 1′.5 in radius centered on the peak of the X-ray emission. A total of 408 (477) events were obtained from GIS2 (GIS3). No significant pulsations were detected in a 2^{23} point fast Fourier transform covering frequencies up to 50 Hz. From empirical results for measurements of pulsed fraction for detected pulsars, we derived an upper limit of $\sim 45\%$ for the pulsed fraction from the entire selected emission region.

If we assume a power-law index $\alpha = 1.5$ (similar to the Crab pulsar) for the point source discussed above, the expected number of counts contributed from this source is 270. This leads to an upper limit of 75% for the pulsed fraction from this source.

Since some pulsars show an increased pulsed fraction at higher energies (Ögelman & Finley 1993), we repeated the above analysis using only events with energies above ~ 2 keV. Again no significant pulsations were detected.

4. EMISSION CHARACTERISTICS

4.1. *Thermal Emission*

While the present *ASCA* observation confirms the nonthermal nature of the central emission from CTA 1, the limited angular coverage does not permit an accurate determination of the total luminosity of this emission component. Further, although the presence of a soft, probably thermal, component to the remnant emission has also been confirmed, the current *ASCA* coverage is insufficient to determine the associated emission measure over the entire remnant. As a plausible (if unproved) scenario, we consider the case of a remnant in the Sedov phase of evolution (Sedov 1959) accompanied by a strong synchrotron nebula driven by a central pulsar. Assuming a shell-type geometry for the thermal component, we may scale the thermal emission measure derived from the central region (a small fraction of the shell in projection) to provide an approximation to that of the entire remnant.

The normalization from the spectral fit is $K = \mathrm{EM}/(4\pi D^2)$, where $\mathrm{EM} = \int n_H n_e dV$ is the volume emission measure and D is the source distance. Averaging the results from the two GIS detectors, we measure $K = (1.1^{+1.1}_{-0.5}) \times 10^{13}$ cm^{-5} for the portion of the remnant observed. The Sedov solution provides the radial density distribution from which the volume emission measure can be derived. We integrate this distribution over the observed portion of the remnant in order to calculate an expected value for the spectral fit normalization. Assuming cosmic abundances, this leads to a preshock hydrogen density $n_0 = 3.7 \times 10^{-2} D_{1.4}^{-1/2}$ cm^{-3}, where $D_{1.4}$ is the remnant distance in units of 1.4 kpc (Pineault et al. 1993). The factor of ~ 2

uncertainty in the spectral fit normalization leads to $\sim 40\%$ uncertainty in n_0.

Assuming the soft thermal component corresponds to the emission-measure–weighted temperature for a Sedov remnant (Table 1), the corresponding shock temperature is $T_s = 1.8 \times 10^6$ K. The remnant age is thus $t = 2.0 \times 10^4 D_{1.4}$ yr. This leads to an explosion energy $E_{SN} = 0.6 \times 10^{50} D_{1.4}^{5/2}$ ergs and a swept-up mass of $M_{sw} = 32.6 D_{1.4}^{5/2} M_\odot$.

The derived value for n_0 is quite small, but not unrealistic for the location of CTA 1 at $250 D_{1.4}$ pc above the Galactic plane; average $n(z)$ models (e.g., Dickey & Lockman 1990) suggest values $\lesssim 0.1$ cm^{-3} at this height.

The somewhat low explosion energy could be reconciled with the more typical values of ~ 0.5–1×10^{51} ergs if the distance has been underestimated by a factor of ~ 3, although this would decrease the already low calculated value of n_0 by a factor of ~ 1.7. The kinematic distance of 1.4 ± 0.3 kpc (Pineault et al. 1993) is based upon a presumed association between the SNR and a shell of H I emission at velocity between -12 and -20 km s^{-1}. If this association is indeed correct, it would appear difficult to derive an explosion energy considerably larger than 10^{50} ergs. We note, however, that the values derived above are based upon the assumption that the observed electron temperature is representative of the shock temperature. If the electrons and ions have not yet reached temperature equilibrium, then the shock temperature will be larger than assumed. For a remnant as evolved as CTA 1, Coulomb equilibration alone is sufficient to limit the ion/electron temperature ratio to values $\lesssim 2$. At most, therefore, the age could be reduced by $\sim 50\%$ and the resulting explosion energy could increase by a factor of ~ 2.

4.2. *Nonthermal Emission*

The total flux attributable to the nonthermal emission component observed within the central 18.5 of the GIS field of view is $F_X(0.5\text{–}10 \text{ keV}) \approx 2.4 \times 10^{-11}$ ergs cm^{-2} s^{-1}. The associated luminosity is $L_X = 5.6 \times 10^{33} D_{1.4}^2$ ergs s^{-1}. We note that this is a factor of ~ 2.8 smaller than the flux quoted in SSS95 (when the latter is extrapolated to the 0.5–10 keV bandpass). This is the result of a better determination of the spectral index leading to a harder spectrum than previously calculated. If we model the nonthermal spectral component as uniformly filling a spherical volume of uniform density, then the ratio of the flux obtained from a 9.2 circular region (9×10^{-12} ergs cm^{-2} s^{-1}) to that above implies a radius $R_p = 17.7 = 7.2 D_{1.4}$ pc. While in principle the X-ray size may be smaller that the actual size of the plerion, we take R_p to be coincident with the actual radius of the plerion; this also implies that the GIS field of view collects the whole nonthermal flux. We note, however, that PSPC spectral results suggest extension of the nonthermal component beyond this central region. Further spectral studies of the outer remnant regions, at higher resolution, are required to further address this issue.

The presence of a dominant power-law component in the central spectrum of CTA 1 clearly suggests the presence of a central pulsar. We note that source 7 (subsequently identified as J000702+7302.9 in the WGACAT; White, Giommi, & Angelini 1997) from the list of unresolved sources within CTA 1 compiled by SSS95 is located at the position of the peak diffuse X-ray emission seen in Figure 1. Assuming a power-law spectrum with photon index of 1.5 for this source, similar to that of the Crab pulsar, the 0.1–2.4 keV flux is 1.8×10^{-13} ergs cm^{-2} s^{-1} (2.5×10^{-4} photons cm^{-2} s^{-1}), leading to an X-ray luminosity of 4.3×10^{31} ergs s^{-1} at a distance of 1.4 kpc, typical of moderate-aged pulsars. The luminosity ratio between this source and that for the extended synchrotron component would be $\sim 0.8\%$, quite low compared with other pulsar/synchrotron nebula associations.

There also exists an unidentified EGRET source whose position is consistent with the point source at the center of CTA 1. Nolan et al. (1996) identify J0009+73 as a high-energy γ-ray source with a measured flux of $F_\gamma(>100 \text{ MeV}) = (55.5 \pm 8.0) \times 10^{-8}$ photons cm^{-2} s^{-1}. The photon index for the source is 1.58 ± 0.20. Extrapolation of this spectrum back to the *ROSAT* band (0.1–2.4 keV) yields a predicted flux equal to that observed for the point source, if we assume a photon index of 1.41. Alternatively, extrapolation of the plerion flux to the EGRET band (using the observed spectral index of 2.03) predicts a flux which is more than a factor of 10 smaller than the observed EGRET flux. While the nonthermal flux measured with *ASCA* must be considered a lower limit (in that the emission may persist outside the observed region), an increase by such a large factor is inconsistent with strict geometric scaling to the full size of CTA 1. Further, both the *ROSAT* and the *ASCA* data indicate that the strength of the nonthermal component decreases toward the periphery. Finally, a spectral index of 2.03 is inconsistent with the quoted index for the EGRET source; for the plerionic emission to extend from the *ASCA* band to the EGRET band would require a spectral break with a decrease in the spectral index, which seems unlikely. We thus conclude that the EGRET emission is more likely to be associated with the point source.

Such an association also presents difficulties. If the source is indeed a pulsar, then there should be a significant cooling component to the X-ray emission. Indeed, the observed flux is consistent with that expected from standard cooling models, thus leaving little to associate with magnetospheric emission. The EGRET data also indicate that the source is variable at about the 2.2 σ confidence level. Such variability, if real, would be problematic for the association of J0009+73 with a pulsar. We note that the AGN discussed in § 1 is just outside the position error box by Nolan et al. (1996). An association with this source would be consistent with variability.

5. DISCUSSION

The nonthermal emission from CTA 1 is presumably associated with a plerion driven by a central pulsar. We may use the derived thermal and nonthermal characteristics of the remnant to investigate the evolutionary properties of the pulsar and its plerion.

From the luminosity of the nonthermal component described above, the current spin-down energy loss rate of the pulsar, $\dot{E}$, can be derived using the empirical relationship $\log L_X = 1.39 \log \dot{E} - 16.6$ derived by Seward & Wang (1988). Thus, $\dot{E} = 1.7 \times 10^{36} D_{1.4}^{1.4}$ ergs s^{-1}. Using this along with the SNR age derived from the Sedov analysis, we may derive the current spin period (Seward & Wang 1988),

$$P \approx \frac{1.4 \times 10^{23}}{(\dot{E}t)^{1/2}} \approx 0.14 D_{1.4}^{-1.2} \text{ s} ,$$

and the spin-down rate,

$$\dot{P} = \frac{P}{2t} = 1.1 \times 10^{-13} D_{1.4}^{-2.2} \text{ s s}^{-1} .$$

Further, a lower limit for the initial spin period, P_0, is established by the condition that the initial spin energy of the pulsar was less than the thermal energy derived from the Sedov analysis. To see this, consider an initial pulsar spin energy in excess of the blast wave energy; as the pulsar evolves, the energy contributed in the form of magnetic flux would drive the SNR evolution and increase the thermal energy unless the initial pulsar energy loss was strongly imbalanced in favor of particle acceleration (which seems unlikely). Thus, $P_0 > 1.2 \times 10^{-2} D_{1.4}^{-5/4}$ s.

For the magnetic dipole model, we can write

$$\dot{E}\tau^2 = \frac{3I^2c^3}{8a^6B_\perp^2} \approx 10^{61} B_{12}^{-2} \text{ ergs s}^{-1} ,$$

where $a \approx 10^6$ cm is the neutron star radius, I is the moment of inertia, B_{12} is the surface magnetic field at the equator in units of 10^{12} G, and $\tau = P/(2\dot{P})$ is the pulsar characteristic age. Using the above, we find $B_{12} = 3.9 D_{1.4}^{-1.7}$.

We next consider the plerion evolution. The Sedov solution discussed in Section 4.1 leads to a central thermal pressure $P_c = 2.6 \times 10^{-11} D_{1.4}^{-1/2}$ dynes cm^{-2}. The derived age of the remnant is sufficiently large for the reverse shock to have passed the plerion boundary, thus leaving the plerion magnetic pressure in equilibrium with the ambient thermal pressure (Reynolds & Chevalier 1984). This leads to a nebular magnetic field $B = 25 D_{1.4}^{-1/4}$ μG. Assuming a power-law spectrum for electrons injected into the nebula of size $R_p = 17'.7$ (see above), standard synchrotron theory (e.g., Ginzburg & Syrovatskii 1965) yields an energy density $U_e = 3.0 \times 10^{-16} B_{-4}^{-3/2} D_{1.4}^{-1}$ ergs cm^{-3} for the electrons producing the X-ray emission, where B_{-4} is the field strength in units of 10^{-4} G. Using the above field, we find $U_e = 2.4 \times 10^{-15} D_{1.4}^{5/8}$ ergs cm^{-3}. The current magnetic energy density is thus roughly 10,000 times larger than the energy density of the X-ray–emitting electrons. We note that this electron energy density is a lower limit since it corresponds only to those whose flux is produced in the X-ray band. If these electrons represent a large fraction of the total electron energy, this implies a large imbalance with the magnetic energy density at the present epoch. As we discuss below, such an imbalance is consistent with approximate equipartition between particle and magnetic flux input from the pulsar given the synchrotron losses experienced by the particles since injection (Bandiera, Pacini, & Salvati 1996).

If we define p as the fraction of the pulsar spin-down power which appears as magnetic flux injected into the nebula, then we may write

$$\frac{d}{dt}\left(\frac{B^2R_p^4}{6}\right) = p\dot{E}R_p .$$

For magnetic dipole losses from a pulsar, we have

$$\frac{\dot{E}}{\dot{E}_0} = \left(1 + \frac{t}{\tau_0}\right)^{-2} .$$

Let us assume that at times smaller than τ_0 the plerion expansion was approximately linear (i.e., the Sedov phase begins at some later time t_S; see Reynolds & Chevalier 1984), with a typical expansion velocity v_0. Upon integrating to t_S, we find:

$$\frac{B^2R_p^4}{6} = pv_0(\dot{E}_0\tau_0^2)\left[\ln\left(1 + \frac{t_S}{\tau_0}\right) - \left(\frac{t_S}{t_S + \tau_0}\right)\right] .$$

The quantity in brackets lies in the approximate range 1–3 for values of t_S/τ_0 in the range 5–50. Including evolution beyond t_S increases this quantity only slightly ($\sim$25%) since the bulk of the magnetic flux is injected from the pulsar at earlier times; we thus approximate this factor by 2. For times $t \gg \tau_0$, we have $\dot{E}t^2 \approx \dot{E}_0\tau_0^2$. Using the value of $\dot{E}$ from above, along with the age from the Sedov solution, we thus have

$$p \approx 0.21\left(\frac{v_0}{1000 \text{ km s}^{-1}}\right)^{-1} D_{1.4}^{0.1} .$$

Thus, for reasonable values of the expansion velocity ($v_0 \approx$ 1400 km s^{-1} for the Crab), we see that the particle and magnetic flux processes are roughly in equipartition at the time of injection. An exact equipartition is attained if the plerion radius has been underestimated by $\sim$25%.

6. CONCLUSIONS

We have used new observations of CTA 1 carried out with the *ASCA* X-ray observatory to establish the nonthermal nature of the central emission. The observed characteristics are consistent with a synchrotron nebula powered by a central pulsar. The point source J000702+7302.9 resides at the center of the diffuse synchrotron emission and represents a viable candidate for the pulsar based upon position and X-ray luminosity. The possible association of this source with the unidentified γ-ray source J0009+73 adds further interest to more detailed investigations. In particular, high-resolution imaging of the source, with high time resolution, should be carried out to search for evidence of pulsations which would confirm the association. Similarly, a high-sensitivity radio search for evidence of an associated pulsar is of interest.

The *ASCA* observations also support the presence of a weak thermal component which may be associated with shock-heated gas from the ISM. If interpreted as emission from a Sedov phase remnant, CTA 1 appears to represent a curious case of an old remnant, with a Crab-like core, which was produced in a low-energy explosion high above the Galactic plane. Joint consideration of the thermal and nonthermal components suggests a pulsar with a spin period of $0.14 D_{1.4}^{1.2}$ s and a surface magnetic field of $3.9 \times 10^{12} D_{1.4}^{-1.7}$ G. Pressure balance between the plerion and the thermal interior of the SNR yields a nebular magnetic field strength of $25 D_{1.4}^{-1/4}$ μG which implies a large imbalance between the magnetic and electron energy densities at the current epoch, but is consistent with equipartition at the time of injection.

The authors would like to thank Olaf Vancura, Jack Hughes, and Ilana Harrus for helpful discussions and suggestions for the text. K. T. is supported by Research Fellowships of the Japan Society for the Promotion of Science for Young Scientists. R. B. gratefully acknowledges the hospitality of the Smithsonian Astrophysical Observatory during the course of this work. This work was supported in part by the National Aeronautics and Space Administration through contract NAS 8-39073 and grants NAG 5-2638 and NAG 5-3486.

REFERENCES

Bandiera, R., Pacini, F., & Salvati, M. 1996, ApJ, 465, L39
Dickey, J. M., & Lockman, F. J. 1990, ARA&A, 28, 215
Ginzburg, V. L., & Syrovatskii, S. I. 1965, ARA&A, 3, 297
Harrus, I. M., Hughest, J. P., Singh, K. P., Koyama, K., & Asaoka, I. 1997, ApJ, submitted
Nolan, P. L., et al. 1996, ApJ, 459, 100
Ögelman, H., & Finley, J. P. 1993, ApJ, 413, L31
Pineault, S., Landecker, T. L., Madore, B., & Gaumont-Guay, S. 1993, AJ, 105, 3, 1060
Pineault, S., Landecker, T. L., Swerdlyk, C. M., & Reich, W. 1997, A&A, in press
Raymond, J. C., & Smith, B. W. 1977, ApJS, 35, 419
Reynolds, S. P., & Chevalier, R. A. 1984, ApJ, 278, 630
Rho, J.-H., Petre, R., Schlegel, E. M., & Hester, J. J. 1994, ApJ, 430, 757
Sedov, L. 1959, Similarity and Dimensional Methods in Mechanics (New York: Academic)
Seward, F. D., Schmidt, B., & Slane, P. 1995, ApJ, 453, 284
Seward, F. D., & Wang, Z-R. 1988, ApJ, 332, 199
Smith, A., Jones, L. R., Peacock, A., & Pye, J. P. 1985, ApJ, 296, 469
Torii, K., Tsunemi, H., Kinugasa, K., & Slane, P. 1997 in X-ray Imaging and Spectroscopy of Cosmic Hot Plasmas, ed. F. Makino & H. Mitsudo (Tokyo: Universal Academy), 395
Yamauchi, S., Kaneda, H., Koyama, K., Makishima, K., Matsuzaki, K., Sonobe, T., Tanaka, Y., & Yamasaki, N. 1996, PASJ, 48, L15
White, N. E., Giommi, P., & Angelini, L. 1997, in preparation

ASCA Observation of the Crab-Like Supernova Remnant 3C58

Ken'ichi TORII,[1] Patrick O. SLANE,[2]

Kenzo KINUGASA,[3] Kiyoshi HASHIMOTODANI,[4] and Hiroshi TSUNEMI[4,5,1]

[1] *NASDA TKSC SURP, 2-1-1 Sengen, Tsukuba, Ibaraki, 305-8505, Japan*

E-mail (KT) torii.kenichi@nasda.go.jp

[2] *Harvard-Smithsonian Center for Astrophysics, 60 Garden Street Cambridge, MA 02138, USA*

[3] *Gunma Astronomical Observatory,*

6860-86 Nakayama, Takayama, Agatsuma,Gunma, 377-0702, Japan

[4] *Department of Earth and Space Science, Graduate School of Science, Osaka University,*

1-1, Machikaneyama-cho, Toyonaka, Osaka, 560-0043, Japan

[5] *CREST, Japan Science and Technology Corporation (JST)*

December 21, 2000

Abstract

We present here the X-ray observation of a Crab-like supernova remnant (SNR) 3C58 with ASCA. We find that the integrated energy spectrum over the nebula is consistent with previous results, showing a power-law spectrum with the photon index $\gamma = 2.2 - 2.4$ modified by interstellar absorption of about $(3 - 4) \times 10^{21}\mathrm{cm}^{-2}$. Inclusion of a blackbody component which is attributable to the central compact source significantly improves the spectral fit. Stringent upper limits for any line emitting thin hot plasma are established. We find for the first time that the nebular spectrum is harder in the central part of the SNR, becoming softer toward the periphery, while the absorption column is uniform across the nebula. Correspondingly, the nebular size decreases with increasing photon energy which is a steeper function of radius than that of the Crab nebula. The results are compared with

synchrotron energy loss models and the nature of the putative pulsar is discussed. Timing analysis was performed to search for pulsed X-ray emission from the central compact source. No significant pulsations are observed, and we present the upper limit for the pulsed fraction.

1 Introduction

The source 3C58 (G130.7+3.1) is believed to be the remnant of a historical supernova (SN) event in A.D. 1181 (e.g., Panagia, Weiler 1980). It shows a center-filled morphology both in the radio (e.g., Reynolds, Aller 1988) and X-ray bands (e.g., Becker et al. 1982). X-ray observations reveal a point-like source in the midst of the nebula (Becker et al. 1982) which contributes 7% of the total flux in the ROSAT HRI energy band (0.1-2.4 keV) (Helfand et al. 1995). The radio spectrum of the nebula is a power-law with an energy index of 0.1 (Green 1986) and the X-ray spectrum is a power-law with an energy index of 1.19 ± 0.12 (Asaoka, Koyama 1990). Though the central object itself is radio quiet, a wisp-like structure elongated in the north-south direction lies only 2.6 arcseconds west of the X-ray compact source (Frail, Moffett 1993). Similar wisp-like structures in the vicinity of the central objects are often found in the Crab-like SNRs, not only in the radio band (Bietenholz et al. 1991; Frail, Moffett 1993) but also in the optical band (Hester et al. 1995). These structures are believed to be associated with the termination of the relativistic pulsar wind by the ambient pressure. These characteristics, along with the nonthermal nature of the extended emission in 3C58, imply that the central source is a neutron star even though no coherent pulsations have been detected at any wavelength to date. From these characteristics, 3C58 is classified as a Crab-like SNR or a *plerion* (Weiler, Panagia 1978).

Though the Crab nebula and 3C58 have much in common, there are considerable differences as well. The radio and X-ray luminosities for 3C58 are factors of ~ 10 and ~ 2000, respectively, below those of the Crab nebula (Helfand et al. 1995). As these objects are powered by the rotational energy loss of the central neutron star, the differences found in the surrounding nebulae should give insights into the properties of the young neutron stars.

The modeling of the Crab-like synchrotron nebulae has evolved with a strong bias on the Crab nebula itself due to its outstanding brightness. Models have been developed to explain the multi-wavelength spectrum and its evolution (e.g., Pacini, Salvati 1973; Reynolds, Chevalier 1984; Reynolds, Chanan 1984; Bandiera et al. 1996), the flow of relativistic particles and the corresponding morphology of the nebula (e.g., Rees, Gunn 1974; Aschenbach,

Brinkmann 1975; Kennel, Coroniti 1984a, b; Chiueh, Li, Begelman 1998). Following the model of Rees and Gunn (1974), Kennel and Coroniti (1984a, b hereafter KCa, b) proposed a magnetohydrodynamical (MHD) flow model with a standing shock having an extremely low magnetization parameter, σ (the ratio of the Poynting to particle energy fluxes in the upstream wind). This model successfully explains the previously observed variation in nebular size with energy from the optical to the hard X-ray band under the suitable boundary conditions.

The distance to 3C58 was derived by H I observations by several authors (Goss et al. 1973; Williams 1973; Green, Gull 1982; Roberts et al. 1993). Following the discussions made by Roberts et al. (1993), we adopt 3.2 kpc throughout this paper.

In this paper, we report the X-ray observation of 3C58 with the spectro-imaging detectors on board ASCA in the energy range 0.5–10 keV.

2 Observation and Data Reduction

3C58 was observed by ASCA (Tanaka et al. 1994) from 12 to 14 in September, 1995. As well as a proposed target of the AO3 observing phase, it was observed as an SIS (Solid-state Imaging Spectrometer) (Burke et al. 1994) calibration source. These observations were carried out with four different satellite attitudes. The fourth observation was made to obtain the accurate background in the adjacent region of the object. The SIS was operated in 1CCD mode with a read-out cycle of 4 s. The Gas Imaging Spectrometer (GIS), a position sensitive gas scintillation proportional counter (Ohashi et al. 1996; Makishima et al. 1996), was operated in PH mode. To search coherent pulsations, portions of the observation were carried out in a mode which allocates more bits to timing resolution than for standard observations. This sacrifices some spatial and spectral resolution. The time resolution of the GIS for the first observation was 1/16 s for high bit rate and 1/2 s for medium bit rate. For the other observations, the resolution was 1/1024 s and 1/128 s for high and medium bit rate, respectively. The observation date and the observation mode are summarized in table 1.

The raw data were screened with the standard screening parameters. The screening criteria restrict events to those obtained outside the South Atlantic Anomaly (SAA), for which the cut-off rigidity is > 6 GeV/c, and for which the angle of the source from the Earth rim is restricted to > 5 deg for the GIS, > 10 deg (25 deg) for the SIS for the dark (bright) Earth rim angle. For the SIS, flickering pixels are removed, only grades 0, 2, 3, and 4 are

selected, and four readout cycles are removed after the satellite passage of the SAA as well as after the satellite passage of the day-night transition. The effective exposure time after the data reduction is summarized in table 2 for each observation.

3 Results

3.1 Energy Spectrum of the Whole Remnant

We first investigated the energy spectrum of the whole SNR, including the compact source. To check the consistency between the detectors, energy spectra were extracted for each detector of each sensor using photons within 4 arcminutes from the emission center. The spectra were fitted with a power-law function modified by the interstellar absorption (Morrison, McCammon 1983). A formally acceptable fit was obtained for each data set by using this model. Since we found no significant systematic deviation above the level of the current status of the detector calibration of ASCA, we fitted the spectra from each observation simultaneously to improve the statistics. We show representative spectra in figure 1 and the best-fit spectral parameters are summarized in table 3.

Becker et al. (1992) obtained $\gamma = 1.5\ ^{+0.5}_{-0.2}$ and $N_{\rm H} = (1.8 \pm 0.5) \times 10^{21}{\rm cm}^{-2}$ with the Einstein SSS, but a somewhat steeper power-law index ($\gamma = 2$) and approximately twice the column density using the IPC.

By fixing the absorption column to $N_{\rm H} = 1.8 \times 10^{21}{\rm cm}^{-2}$, the value determined with the Einstein SSS, Davelaar et al. (1986) obtained $\gamma = 2.30 \pm 0.26$ with the EXOSAT ME. Asaoka and Koyama (1990) obtained $\gamma = 2.19 \pm 0.12$ and $N_{\rm H} < 10^{21.5}{\rm cm}^{-2}$ with the Ginga LAC. Helfand et al. (1995) derived $\gamma = 1.70 \pm 0.30$ and $N_{\rm H} = (3.25 \pm 0.7) \times 10^{21}{\rm cm}^{-2}$ for the nebula by considering the Einstein SSS, IPC, ROSAT HRI, and the 21 cm (Green, Gull 1982) measurements, and a blackbody of 3.5×10^6 K for the central compact source. Taking into account the statistical and systematic errors of the data in the literature, these values are in reasonable agreement with those summarized in table 3. By using the first set of the SIS data, the observed flux is $1.3 \times 10^{-11}{\rm ergs \cdot s^{-1} \cdot cm^{-2}}$ and the unabsorbed flux is $1.9 \times 10^{-11}{\rm ergs \cdot s^{-1} \cdot cm^{-2}}$ in the range 0.5–10 keV. The statistical error in the flux determination is about 4% and the systematic error for the absolute flux is about 10%. The corresponding luminosity is $2.4 \times 10^{34} d^2_{3.2{\rm kpc}} {\rm ergs \cdot s^{-1}}$ in the range 0.5–10 keV.

Though we see no line structure in the raw energy spectra by eye, we might expect some amount of thermal plasma of temperature $\sim 10^7$K that is shock-heated at the outgoing blast wave, and possibly at the reverse shock. To

search for evidence of such thermal emission, we performed the following analysis to establish limits on the emission measure (EM $= \int n_e n_H dV$, where n_e, n_H, and V denote the electron number density, the hydrogen number density, and the volume, respectively) by using a thin thermal plasma emission code.

We used the MEKAL model in XSPEC ver.9.0 which calculates the emission from an optically thin thermal plasma in collisional ionization equilibrium. The model includes line emission from heavy elements based on the model calculations of Mewe and Kaastra (e.g., Mewe et al. 1985) with the Fe L calculations by Liedahl et al. (1995). We assumed heavy elemental abundances equal to the solar values of Anders and Grevesse (1989). All the SIS and GIS data were used simultaneously to obtain the stringent upper limit. If both the power-law index and the absorption are allowed to vary, along with the thermal component, we find large absorption and a large power-law index which is incompatible with the Ginga result at higher energy (Asaoka, Koyama 1990). Therefore, we fix the power-law index and the absorption to be the best-fit values obtained without the thermal component. The resultant upper limit of the EM is shown in the upper panel of figure 2 for the assumed temperature range 0.1–12.8 keV. The corresponding upper limit of the rms density of the thermal plasma is shown in the lower panel assuming a spherical volume whose angular radius is 4 arcminutes. The solid line shows the limit when the filling factor is 1/4 which corresponds to the Sedov type self similar solution (Sedov 1993) and the dashed line shows the limit for a uniform sphere and the filling factor of unity.

Another possible thermal component is blackbody radiation from the cooling neutron star surface. A blackbody temperature of about 10^6K from the entire surface, or an even higher temperature due to polar cap heating, may be expected (e.g., Yancopoulos et al. 1994; Slane 1994; Slane, Lloyd 1995; Helfand et al. 1995). Helfand et al. (1995) derived a crude constraint on the spectral shape of the compact source based on the flux ratio between the Einstein HRI and the ROSAT HRI. They obtained a blackbody temperature of 3.5×10^6K and an emitting area of $\sim 4.5 \times 10^{10} d^2_{3.2\mathrm{kpc}}$ cm^2. To examine this component, we introduced a blackbody component to the simultaneous fit of all the SIS and GIS spectra. Without the blackbody component, the photon index, normalization of the power-law component, and the absorption column are $\gamma = 2.29 \pm 0.03$, $N = (4.8 \pm 0.2) \times 10^{-3}$ photons $\cdot$ s^{-1} $\cdot$ keV^{-1} $\cdot$ cm^{-2} at 1 keV, and $n_H = (4.0 \pm 0.2) \times 10^{21}$cm^{-2} with χ^2/d.o.f. = 1487/1330. With the blackbody component, χ^2/d.o.f. = 1474/1328 which shows that the blackbody component is significant at 99.7% level according to F-test. The best-fit spectral parameters are $T_{\mathrm{blackbody}} = (5.1\ ^{+0.6}_{-0.5}) \times 10^6$ K and the emitting area of $(1.2\ ^{+0.8}_{-0.7}) \times 10^{10} d^2_{3.2\mathrm{kpc}}$ cm^2. The parameters for the power-law component and the absorption column are $\gamma = 2.1 \pm 0.1$, $N = (3.6 \pm 0.6) \times$

10^{-3} photons $\cdot s^{-1} \cdot keV^{-1} \cdot cm^{-2}$ at 1 keV, and $n_H = (3.3 \pm 0.4) \times 10^{21} cm^{-2}$. With this model, the observed flux from the power-law and the blackbody component is 1.1×10^{-11} and 8.4×10^{-13}ergs $\cdot s^{-1} \cdot cm^{-2}$ in the 0.5–10 keV range, respectively. The unabsorbed flux is 1.6×10^{-11} and 1.2×10^{-12}ergs $\cdot s^{-1} \cdot cm^{-2}$, respectively. The corresponding luminosity is $L_{X,pow} = 2.0 \times 10^{34} d^2_{3.2kpc}$ergs $\cdot s^{-1}$ and $L_{X,blackbody} = 1.5 \times 10^{33} d^2_{3.2kpc}$ergs $\cdot s^{-1}$. We find the blackbody temperature derived here is ~ 1.5 times higher than that of Helfand et al. (1995) and the emitting area is ~ 3.8 times smaller. From the flux point of view, however, these two results are remarkably consistent within $\sim 20\%$. Thus we have confirmed the presence of a relatively high temperature blackbody component (Helfand et al. 1995) in the spectrum of the whole SNR. Due to the limited spatial resolution of ASCA and the limited spectral resolution of Einstein HRI and Rosat HRI, the temperature of the blackbody component can not be strictly constrained. The contribution from the blackbody component is further examined in the following spatially resolved analyses to confirm that it predominantly comes from the central compact source.

The power-law component of the X-ray spectrum determined with the power-law plus blackbody model is shown in figure 3 together with the radio (Green 1986; Salter et al. 1989 and the references therein), infrared (Green, Scheuer 1992; Green 1994), and γ-ray (Fichtel et al. 1994) data. The infrared and γ-ray data are the upper limits. The multi-wavelength spectrum of the Crab nebula is also shown in the figure for comparison (e.g., Saken et al. 1992; Wu 1981 and the references therein).

3.2 Energy Spectra of Concentric Annular Regions

The synchrotron lifetime of the electrons producing the X-ray emission varies as $\propto E^{-1}$. We thus expect a radial variation in the spectral index of the nebula with emission in the inner regions (where electron injection is most recent) exhibiting a flatter spectrum than for the outer regions. To investigate such a scenario, we performed spatially resolved spectral analysis. As the SIS has better spatial resolution than the GIS, we used only the SIS data for this analysis. We extracted energy spectra from concentric annular regions centered on the emission peak. The width of each annulus was 1 arcminute and the outer radii were 1, 2, 3, and 4 arcminutes. We first used a power-law function modified by the interstellar absorption to examine the systematic effect in the procedure and then introduced a blackbody component to the fit.

Since the point spread function (PSF) of ASCA X-ray telescope (XRT) (Serlemitsos et al. 1995) has a half power diameter of about 3 arcminutes, comparable in size with the 3C58 extended nebula, we conducted the analysis in the

following way to avoid the possible systematic effects. We first fitted the 3C58 data with all the model parameters free. We found that the power-law index was the flattest in the central region, steepening toward the periphery, while the absorption column was uniform across the nebula. To see the possible systematic effects, we applied the same procedure to the archival data of 3C273 (sequence number 71038020), a bright point source. We found neither the systematic steepening of the power-law index nor any systematic change of the absorption column depending on the radius. Since we found no significant systematic effects due to the instrumental response functions, we fitted the 3C58 data with the absorption column and the blackbody temperature (when included) fixed at the best-fit value obtained for the whole remnant to obtain statistically stringent limit on the other spectral parameters.

The resultant power-law indices are shown in figure 4 with 90% confidence errors. Squares show the result without the blackbody component and the circles show the result with the blackbody component. We find significant softening of the energy spectrum toward the periphery of the nebula, as expected from the synchrotron energy loss of the relativistic particles. Also, when the blackbody component is included, we find that the fraction of the flux from the blackbody component is about 10% in the inner part while it becomes negligibly weak at the outermost annulus (9.4%, 9.7%, 4.0%, and $< 0.6\%$ in the 0.5–10 keV range from the innermost toward the outermost annulus). This supports the interpretation that the blackbody radiation comes from the central source in 3C58. Thus we have shown that the spectrum consists of two components, one the spatially extended power-law component and the other a blackbody component at the center, and the former shows softening toward the periphery of the nebula. Since the spectral indices derived here are obtained after the convolution by the XRT PSF, we further quantify this softening in the following section in terms of the energy-size relation.

3.3 Image Fitting Analysis

In the method we adopted in the previous section, the spectrum for a given annulus is contaminated by the photons originating from the adjacent annuli due to the wings of the XRT PSF. In this section, we explore the spatial distribution of the energy spectrum using a different approach. We have extracted images in several energy ranges and fitted them with some appropriate function convolved by the PSF. In this method, the extracted image of each energy range does not suffer much from the photons whose energy is out of the energy range considered. This is justified for the SIS data due to its high energy resolution. We used subroutines and the standard calibration files provided by the instrumental team as part of the *jbldarf* and *ftools* packages to calculate the PSF. The azimuthal

structures due to the telescope quadrants are not taken into account in the PSFs in these functions.

Since we confirmed the blackbody component in the spectrum which is attributable to the compact source at the center of the nebula, we utilize a model function which comprises the nebula component, the compact source component, and the background component. We employ broad and narrow Gaussians for the compact source and the nebula, respectively. The model function is expressed as follows.

$$f(x,y) = A \cdot \exp(-\frac{(x-x_0)^2}{2\sigma_{1x}^2} - \frac{(y-y_0)^2}{2\sigma_{1y}^2}) + B \cdot \exp(-\frac{(x-x_0)^2}{2\sigma_{2x}^2} - \frac{(y-y_0)^2}{2\sigma_{2y}^2}) + C \quad (1)$$

where A, B, and C are the normalizations for the nebula, the compact source, and the background component, respectively; x and y are the positions in the right ascension and declination coordinate. Since the major axis of the nebular emission is well aligned in the east-west direction, we did not rotate the function around the center. The size of the nebula is characterized by σ_{1x} and σ_{1y}. σ_{2x} and σ_{2y} are fixed at 5 arcseconds which we find are appropriate to reproduce a compact source at the center. Since the contribution from the blackbody component to the observed flux is, based on the best fit spectral parameters, 7.9%, 15.6%, 16.7%, and 2.0% in the 0.5–1, 1–1.5, 1.5–3, and 3–10 keV range respectively, the ratio between A and B is fixed for each energy range to reproduce these fractions.

To examine the systematic error of the XRT PSF, we fitted the 3C58 images by using the 3C273 image as a PSF. A similar energy-size relation was obtained, but the derived sizes were different by +4%, +11%, +14%, and +11% in the EW direction and -6%, -8%, -11%, and -20% in the NS direction, in the 0.5–1, 1–1.5, 1.5–3, and 3–10 keV range, respectively. Thus we found at most 20% systematic error between the analyses made with the two kinds of PSFs. Since these systematic errors dominate the statistical errors, we quote 20% as the total error.

Figure 5 shows the azimuthally averaged radial profile of the data, the convolved model function, and the PSF. Figure 6 shows the position of the Gaussian center. Error bars show the 90% confidence positional uncertainty of ASCA which is 40 arcseconds (Gotthelf 1996; Gotthelf, Ishibashi 1997). We noted that the central position of the concentric annular regions used in the previous analyses agreed with the Gaussian centers within ~ 0.1 arcminutes. The absolute value of the Gaussian center is displaced about 40 arcseconds to the east compared with the position of the compact source determined by ROSAT HRI (Helfand et al. 1995), an offset which is consistent with the systematic positional uncertainty.

Figure 7 shows the size of the nebula as a function of the observing photon energy. The nebular size is found to show a monotonic decrease toward higher energy. A power-law fit for the nebular size as a function of the energy

yields

$$r_{\rm FWHM}[\rm arcsec] = (190 \pm 40) \times E[\rm keV]^{-(0.5\pm0.2)} \quad (2)$$

in the east-west direction and

$$r_{\rm FWHM}[\rm arcsec] = (140 \pm 30) \times E[\rm keV]^{-(0.5\pm0.2)} \quad (3)$$

in the north-south direction.

3.4 Timing Analysis

Though the emission characteristics of 3C58 strongly indicate the presence of a central pulsar, to date no coherent pulsations from the central object have been reported (Helfand et al. 1995). To search for a periodic signal from the central object, we performed a power spectral density (PSD) analysis on the GIS data. Photons extracted within 4 arcminutes from the emission center were used in the analysis. Barycentric corrections were made to the photon arrival times and a fast Fourier transformation (FFT) was applied to obtain the PSD. To improve the statistics, GIS2 and GIS3 data were co-added and they were analyzed by using a software developed by ourselves (e.g., Torii et al. 1997).

We found no significant pulsations at the 99% confidence level in the frequency range 0.01–64 Hz. The higher frequency range was limited by the time resolution of medium bit rate data. The upper limits for the pulsed fraction for a sinusoidal pulse shape were calculated according to the method described by Vaughan et al. (1994). The resultant 99% confidence upper limits for the entire selected region are summarized in table 4 for the three energy ranges, 0.7–10, 0.7–2, and 2–10 keV.

Since the number of photons is dominated by those originating from the nebula, with only $\sim$ 10% originating from the central compact source, the pulsed fraction of the compact source is not tightly constrained. For the whole energy band (0.7–10 keV), the fraction of photons from the blackbody component expected from the best-fit spectral parameters is 11.7%. Therefore, if the blackbody component is pulsating, the upper limits for the pulsed fraction of the compact source are estimated as 62%, 82%, 80%, and 74% in the 0.01–1, 1–8, 8–32, and 32–64 Hz range, respectively.

4 Discussion

4.1 Multi-Wavelength Spectrum

Using the multi-wavelength spectrum of 3C58 shown in figure 3, we may investigate the time dependent energy loss properties of the nebula. In the following discussions we use the relation $F_{\rm X}[{\rm Jy}] = 10^{13.5} \cdot \nu[{\rm Hz}]^{-1.1}$ derived from the best-fit spectral parameters of power-law plus blackbody model. This relation is shown by a dotted line in figure 3. For comparison between the Crab nebula and 3C58, we have summarized the basic parameters of these two objects in table 5.

As noted by Green and Scheuer (1992) (hereafter GS), a sharp break must exist around 5×10^{10} Hz by comparing the radio data with the infrared data, below which the relation $F_{\rm R}[{\rm Jy}] = 10^{2.3} \cdot \nu[{\rm Hz}]^{-0.09}$ is applicable. Extrapolation of the X-ray spectrum back toward lower energies yields a flux density below the upper limits from IRAS data (Figure 3). However, standard synchrotron loss models for a power law distribution of electrons predict a radiated spectrum whose index beyond the break is 0.5 larger than the radio spectral index of ~ 0.1. The fact that the X-ray energy index is much larger than 0.6 clearly rules out a single break under such a scenario.

Based on the energy loss model of Pacini and Salvati (1973), Bandiera et al. (1996) proposed that the low frequency spectral break for the plerionic component of the SNR G11.2-0.3 be identified with $\nu_{\rm c}$, a break associated with the radiative lifetime at τ, a characteristic slowing-down time scale of the pulsar, rather than $\nu_{\rm b}$, the break frequency associated with the radiative lifetime at the current time t (Pacini, Salvati 1973; Reynolds, Chanan 1984; Bandiera et al. 1996; Woltjer et al. 1997). If the break at $\nu \simeq 50$ GHz for 3C58 is due to the radiative lifetime at the current time, an unreasonably large magnetic field of $\gtrsim 3 \times 10^{-3}$ G has to exist in the nebula. We thus interpret this break as due to the decreasing energy output from the pulsar. However, a simple model does not reproduce the whole electromagnetic spectrum from radio through gamma-ray, and fine tuning of pulsar's braking law and the nebular expansion law seems to be needed (e.g., Reynolds, Chanan 1984). Further, if a second spectral break is invoked, it would still need to be at frequencies below $\sim 10^{12}$ Hz in order to be compatible with the IR upper limits. Woltjer et al. (1997) have shown that the sharpness of these breaks cannot be reproduced by any standard evolutionary scenario with a fixed braking index. Instead, their results support the suggestion by GS that a sudden reduction in the particle injection rate is required at some point in time.

Difficulties in reproducing the detailed spectra of plerionic remnants based on a single power-law particle distribution are well-known (Reynolds, Chevalier 1984; Reynolds, Chanan 1984; Atoyan, Aharonian 1996; Kennel,

Coroniti 1984a, b). In addition to an inherent change in the particle injection spectrum, there are other possible mechanisms which can lead to spectral breaks. In particular, the presence of multiple particle populations with different spectral properties can lead to such features. Such a scenario has some observational support. Fürst et al. (1988) observed the Crab-like SNR G21.5–0.9 at 22.3 GHz and compared the result with the Einstein HRI map previously obtained by Becker and Szymkowiak (1981); they noted that maximum X-ray emission coincides with a minimum in the radio emission. Recent *Chandra* observations of G21.5–0.9 (Slane et al. 2000) confirm the bright compact central X-ray emission, thus indicating a difference in the spatial distribution of at least some of the radio and X-ray producing particles. These results seem to suggest complex injection processes for radio and X-ray producing particles. However, we can not yet say whether this scenario holds for 3C58 with the currently available data.

4.2 Central Object

Observationally, a variety of X-ray spectra and pulse profiles have been reported for known rotation powered pulsars. Some show small duty cycle pulses with large pulsed fractions while others show sinusoidal pulse profiles with small pulsed fractions (e.g., Ögelman et al. 1993; Finley et al. 1992; Halpern, Ruderman 1993). Also, pulsed fractions are known to vary with photon energy.

If the X-ray spectrum of the pulsed component of the compact object in 3C58 is the same as that of the blackbody component determined from the spectral analysis, upper limits for the pulsed fraction of the compact source are obtained as 62–82% in the 0.7–10 keV band depending on the frequency range as described above. On the other hand, if the pulsed emission is hard, we may expect the number fraction of photons from the compact source to increase with increasing energy. From the simultaneous fit of all the SIS and GIS data using two power-law models modified by the interstellar absorption, of which one component has a photon index fixed at that for the Crab pulsar ($\gamma = 1.7$; Lyne, Graham-Smith 1990), we obtained an upper limit of 13% of the total counts for the number fraction from this component. Using this value, upper limits for the pulsed fraction for the compact source, in the case of the flat pulsar spectrum, are obtained as 56%, 74%, 72%, and 67% in the 0.01–1, 1–8, 8–32, and 32–64 Hz range, respectively, in the whole energy band (0.7–10 keV).

Helfand et al. (1995) obtained a blackbody temperature (3.5×10^6K) and an emitting area ($\sim 4.5\times10^{10} d^2_{3.2\mathrm{kpc}}\mathrm{cm}^2$) for the central compact source. They found that the temperature is higher than that expected from any current

cooling models (e.g., Nomoto, Tsuruta 1987; Page, Applegate 1992) and that the associated emitting area is smaller than that expected from the whole neutron star surface. Therefore, they attributed the emission to a heated polar cap. We have confirmed the existence of a blackbody spectrum with the temperature of $T_{\rm blackbody} = (5.1\ ^{+0.6}_{-0.5}) \times 10^6$ K and the emitting area of $(1.2\ ^{+0.8}_{-0.7}) \times 10^{10} d^2_{3.2{\rm kpc}}$ cm^2.

We can infer some of the properties if the neutron star by considering the empirical relationship between the X-ray luminosity, L_X, of pulsar/plerion systems and the spin-down power, $\dot{E}$, of the central pulsar derived by Seward and Wang (1988) based upon observations with the Einstein Observatory: $\log L_X = 1.39 \log \dot{E} - 16.6$. Adopting this relationship for 3C58, and converting the unabsorbed ASCA (0.5-10 keV) flux to the Einstein IPC bandpass (0.2-2.4 keV) for which the relationship was derived, we obtain $\dot{E} \sim 4 \times 10^{36} d^2_{3.2{\rm kpc}}$ ergs s^{-1}. This value of $\dot{E}$ is two orders of magnitude smaller than that for the Crab pulsar, clearly indicating that not all young neutron stars are "Crab-like" in terms of their spin-down characteristics.

Assuming that the pulsar has spun down significantly from its initial period and has lost its rotational energy at the rate of the pure magnetic dipole radiation, the SNR age (814 yr assuming an association with SN 1181) and energy loss rate can be used to estimate the initial spin period (Seward and Wang 1988):

$$P = \left(\frac{2\pi^2 I}{\dot{E} t} \right)^{1/2} \approx 0.44 d_{3.2}^{-0.7} \ {\rm s}. \tag{4}$$

The spin-down rate is then $\dot{P} \sim 8.5 \times 10^{-12} d_{3.2}^{-1}$ s s^{-1} and the surface magnetic field strength is $B \approx 6 \times 10^{13} d_{3.2}^{-0.7}$ G, which is at the high end of magnetic field values for the population of young pulsars. We note that variations as large as a factor of 10 or so are observed in the L_x vs. $\dot{E}$ relationship, which could result in an overestimate of the field strength of more than a factor of 3. More importantly, relaxing the assumption that the initial spin period was much shorter than the current period leads to a broad range of permissible magnetic fields.

If the emitting area inferred from the blackbody component described above corresponds to a standard dipole-geometry polar cap, we may follow another path toward determining the spin properties of the central object (Helfand et al. 1995, equation (4); Lyne, Graham-Smith 1990, equation (14.7))

$$P = 58[{\rm ms}] (\frac{r_{\rm cap}}{0.6{\rm km}})^{-2} (\frac{R_*}{10{\rm km}})^3 \cos^2(90^\circ - \theta). \tag{5}$$

The notations are basically the same as those of Helfand et al. (1995); $r_{\rm cap}$ is the polar cap radius, R_* is the neutron

star radius, θ is the angle between the rotation and magnetic axes, and the units are in cgs unless otherwise specified. The spin down rate is thus $\dot{P} = 1.1 \times 10^{-12}[\mathrm{s \cdot s^{-1}}](\frac{r_{\rm cap}}{0.6\mathrm{km}})^{-2}(\frac{R_*}{10\mathrm{km}})^3 \cos^2(90^\circ - \theta)$, and the current spin down power of the pulsar is $\dot{E} = 2.3 \times 10^{38}[\mathrm{ergs \cdot s^{-1}}](\frac{I_*}{10^{45}})(\frac{r_{\rm cap}}{0.6\mathrm{km}})^4(\frac{R_*}{10\mathrm{km}})^{-6} \cos^{-4}(90^\circ - \theta)$.

The conversion rate of the spin down power to the power-law X-ray luminosity is

$$\frac{L_{\rm X}}{\dot{E}} = 9 \times 10^{-5}(\frac{L_{\rm X,pow}}{2.0 \times 10^{34}})(\frac{I_*}{10^{45}})^{-1}(\frac{r_{\rm cap}}{0.6\mathrm{km}})^{-4}(\frac{R_*}{10\mathrm{km}})^6 \cos^4(90^\circ - \theta) \quad (6)$$

which is anomalously low compared to other young objects (Seward, Wang 1988; Becker, Trümper 1997; Kawai, Tamura, Shibata 1998). This again leads to a relatively strong magnetic field ($\sim 10^{13}$ G), but we note that the $\dot{E}$ result depends very strongly on the inferred polar cap size, which is quite uncertain. In particular, one of the uncertainties is the spectral fit by a simple blackbody model. More realistic models have been constructed and applied to several neutron star candidates (e.g., Zavlin, et al. 1996; Zavlin, et al. 1998). These models give a factor of $\simeq 2$ lower temperature and a factor of $\gtrsim 4$ larger emitting radius, values which are still too hot and too small to reconcile with emission from the entire surface of a neutron star. In the discussion below, we adopt the value of $\dot{E}$ derived from the Seward & Wang (1988) relationship under the assumption that the spin-down power of the source in 3C58 is similar to that of other objects powering synchrotron nebulae.

4.3 Energy-Size Relation and the Particle Flow in the Nebula

The measured size of 3C58, and its dependence on energy, can be used to derive constraints on the particle flow in the nebula. The overall picture is as follows (see, e.g., KCa). A central pulsar injects energy into the nebula at a rate $\dot{E}$ in the form of a relativistic particle wind. The wind zone is bounded by an MHD shock at a radius r_s beyond which the bulk particle flow is decelerated and the pressure is increased. A non-relativistic flow transports plasma and magnetic flux from the shock region to the edge of the nebula. Synchrotron emission from decelerated particles in a primarily toroidal magnetic field forms the observed nebula. Equipartition pressure of the magnetic field and the particle energy density drives the nebular expansion and determines the nebular structure. In this picture, an important parameter which characterizes the system is the magnetization parameter, σ, the ratio of the Poynting to particle energy fluxes in the upstream wind. The parameter can be constrained by applying pressure and flow boundary conditions at the edge of the nebula.

From radio observations (GS), the equipartition pressure in the nebula is estimated to be $P_{\rm neb} \sim 10^{-10}$ dyn cm^{-2},

which is also two orders of magnitude smaller than in the Crab nebula. The corresponding magnetic field of the nebula is $\sim 5 \times 10^{-5}$ G. Balancing the ram pressure of the wind, $\dot{E}/(4\pi c R_s^2)$, with the internal pressure of the nebula, we estimate that the distance from the pulsar to the confinement shock region is $R_s \sim 0.1$ pc. This corresponds to an angular size of ~ 6.5 arcsec. Using deep VLA imaging, Frail and Moffett (1993) discovered an elongated radio wisp just west of the compact X-ray source, which they argue is the termination shock from the pulsar wind. Using the ROSAT HRI position determination for the X-ray source (Helfand et al. 1995), the wisp lies at a distance of ~ 6.7 arcsec (0.1 pc) from the compact source, in excellent agreement with the above estimates. We note that Frail and Moffett (1993) quote an angular separation of 2.6 arcsec based upon the position determination of the compact source using Einstein HRI data; this difference is consistent with the ROSAT result considering the aspect determination errors of the two satellites. The radio wisp thus lies at a distance consistent with the estimated shock position and appears to represent a distinct signature of the termination shock.

From equation 5.15 of KCa, the magnetization parameter of the wind is related to the velocity profile of the nebula by $v(z) \approx 3\sigma[1 + (3\sigma z^2)^{-1/3}]$ where $z \equiv r/r_s$. The apparent size of the radio nebula ($10'.3 \times 6'.3$) yields a nebular size $r_N = (4.4 - 2.9) d_{3.2}$ pc. It is interesting to note that this yields $r_N/r_s \approx 15 - 100$ which is similar to that for the Crab (~ 20). Using the age of 814 yr thus gives a mean expansion velocity of $(5.4 - 3.5) \times 10^8 d_{3.2}$ cm s^{-1}. Assuming homologous expansion, the current velocity is 2/5 of the averaged value. Thus, using $z_N = r_N/r_s$ we find $\sigma \sim (2 - 6) \times 10^{-3}$, comparable to that for the Crab nebula. Alternatively, constant velocity of expansion leads to $\sigma \sim (6 - 15) \times 10^{-3}$. Thus, the prime assumption of the KC model, namely a small magnetization parameter corresponding to a particle-dominated wind, is valid here.

Well beyond the wind termination shock, the magnetic field in the nebula is primarily the wound-up field from the pulsar. The radial profile of this toroidal field is $B(r) \propto [rv(r)]^{-1}$ (Aschenbach, Brinkmann 1975; Ku et al. 1976). Under the assumption of a power law velocity profile $v(r) \propto r^{-m}$ (Aschenbach, Brinkmann 1975), the magnetic field strength then varies as $B(r) \propto r^{m-1}$. Due to the finite synchrotron lifetime of the emitting electrons, the measured nebular radius is a function of the observed photon energy: $r \propto E^{-1/(6m-2)}$ (Aschenbach and Brinkmann 1975). Using the measured energy dependence of the nebular size summarized in Section 3.3, we find $m = 0.7^{+0.2}_{-0.1}$ for both EW and NS directions. The magnetic field strength thus decreases slowly with radius. For the Crab nebula, Ku et al. (1976) find an energy-size relationship which leads to $m = 1.46^{+0.10}_{-0.08}$. The velocity law is thus flatter for 3C58, indicating a smaller deceleration of the particle flow in the nebula which corresponds with the smaller inferred

confinement pressure for 3C58 relative to that for the Crab.

From the above discussion, we propose a semi-quantitative picture of 3C58 as follows. The current spin-down power of the central pulsar in 3C58 is $\dot{E} \sim 4 \times 10^{36}$ erg s^{-1} which is two orders of magnitude smaller than that of the Crab pulsar. From radio observations, the equipartition pressure in the nebula is $\sim 10^{-10}$ dyn cm^{-2} which is also about two orders of magnitude smaller than for the Crab nebula. Consequently, the position of the standing shock where the ram pressure of the pulsar wind balances the nebular pressure is at about the same distance from the pulsar, $r_s \sim 0.1$ pc, for both 3C58 and the Crab. The magnetization parameter $\sigma \sim (2-15) \times 10^{-3}$ is of roughly the same order as that for the Crab, indicating a particle-dominated flow at the point of injection. Using these parameters, we obtain the upstream magnetic field (KCb, equation 2.2) as $B_1 = 2.6 \times 10^{-6}(\dot{E}/(4 \times 10^{36}$ erg s$^{-1}))^{1/2}(\sigma/(5 \times 10^{-3}))^{1/2}(r_s/0.1$ pc$)^{-1}$ G. The downstream magnetic field is amplified by a factor of 3 for the small σ limit (KCa, equation 4.15d) and $B_2 \sim 7.8 \times 10^{-6}$ G. The magnetic field in the inner regions increases with increasing radius, and reaches the equipartition value of $\sim 5 \times 10^{-5}$ G at a radius $\bar{r} = r_s\bar{z} = r_s(3\sigma)^{-1/2} \sim 0.8$ pc. If we approximate the bulk motion velocity in the nebula by a power law, we find a flatter profile than for the Crab, indicating a slowly decreasing magnetic field strength in the outer nebula and a smaller deceleration with lower confinement pressure in 3C58 than for the Crab.

5 Conclusion

With the broad band spectroscopic capability of ASCA, we have obtained accurate X-ray spectra of the SNR 3C58. Using both the SIS and GIS spectra, we find the integrated emission to be best described by a power law with $\gamma = 2.1 \pm 0.1$ accompanied by a blackbody with $T_{\rm blackbody} = (5.1^{+0.6}_{-0.5}) \times 10^6$ K and an emitting area of $(1.2^{+0.8}_{-0.7}) \times 10^{10} d^2_{3.2}$ cm^2. The column density is $N_H = (3.3 \pm 0.4) \times 10^{21}$ cm^{-2}. We associate the blackbody component with the central compact X-ray source in the remnant. No pulsations are detected from the central emission in 3C58. We set upper limits of $\sim 55-80\%$ for the pulsed fraction of the compact source, depending upon the spectral characteristics of any pulsed emission.

Using images of the nebula in different energy bands, we have established the spectral softening with radius expected for a synchrotron spectrum injected from a central source. We have used these results to obtain, for the first time, the energy-size relation for the 3C58 nebula. By comparing this result to model of Aschenbach and

Brinkmann (1975) we find the bulk motion velocity and the magnetic field strength to be flatter functions of radius than for the Crab nebula. In addition, we have used the results to derive constraints on the interior pressure and magnetic field, as well on the shock magnetization parameter, using the models of KC. Small confinement pressure and the small deceleration of expansion of the 3C58 nebula has been suggested for the 3C58 nebula compared to the Crab.

The authors are grateful to the referee, Dr. Robert Petre, for invaluable comments and suggestions, which largely improved the draft. The authors are grateful to all the members of the ASCA team. KT was supported in part by Research Fellowships of the Japan Society for the Promotion of Science for Young Scientists. POS is supported in part by NASA Contract NAS8-39073 and Grants NAG5-2638 and NAG5-3486.

References

Anders E., Grevesse N. 1989, Geochimica et Cosmochimica Acta 53, 197
Asaoka I., Koyama K. 1990, PASJ 42, 625
Aschenbach B., Brinkmann W. 1975, A&A 41, 147
Atoyan A.M., Aharonian F.A. 1996, MNRAS 278, 525
Bandiera R., Pacini F., Salvati M. 1996, ApJL 465, L39
Becker R.H., Szymkowiak A.E. 1981, ApJL 248, L23
Becker R.H., Helfand D.J., Szymkowiak A.E. 1982, ApJ 255, 557
Becker W., Trddotumper J. 1997, A&A 326, 682
Bietenholz M.F., Frail D.A., Hankins T.H. 1991, ApJL 376, L41
Burke B.E., Mountain R.W., Daniels P.J., Cooper M.J., Dolat V.S. 1994, IEEE Trans. Nuclear Science 41, 375
Chiueh T., Li Z-Y., Begelman M.C. 1998, ApJ 505, 835
Davelaar J., Smith A., Becker R.H. 1986, ApJL 300, L59
Fichtel C.E., Bertsch D.L., Chiang J., Dingus B.L., Esposito J.A., Fierro J.M., Hartman R.C., Hunter S.D. et al. 1994, ApJS 94, 551
Finley J.P., Ögelman H., Kiziloglu U. 1992, ApJL 394, L21
Frail D.A., Moffett D.A. 1993, ApJ 408, 637
Fürst E., Handa T. Morita K., Reich P., Reich W., Sofue Y. 1988, PASJ 40, 347
Goss W.M., Schwartz U.J., Wesselius P.R. 1973, A&A 28, 305
Gotthelf E. 1996, ASCA News 4, p31
Gotthelf E., Ishibashi K. 1997, X-ray Imaging and Spectroscopy of Cosmic Hot Plasmas, ed Makino F., Mitsuda K. (Universal Academy Press, Tokyo) p631
Green D.A., Gull S.F. 1982, Nature 299, 606
Green D.A. 1986, MNRAS 218, 533
Green D.A., Scheuer P.A.G. 1992, MNRAS 258, 833 (GS)
Green D.A. 1994, ApJS 90, 817
Halpern J.P., Ruderman M. 1993, ApJ 415, 286
Helfand D.J., Chanan G.A., Novick R. 1980, Nature 283, 24
Helfand D.J., Becker R.H., White R.L. 1995, ApJ 453, 741
Hester J.J., Scowen P.A., Sankrit R., Burrows C.J., Gallagher III J.S., Holtzman J.A., Watson A., Trauger J.T. et al. 1995, ApJ 448, 240
Kawai, N., Tamura, K., Shibata, S. 1998, Neutron Stars and Pulsars Thirty Years after the Discovery, ed. N. Shibazaki, N. Kawai, S. Shibata, & T. Kifune (Tokyo: Universal Academy Press), 449
Kennel C.F., Coroniti F.V. 1984, ApJ 283, 694 (KCa)
Kennel C.F., Coroniti F.V. 1984, ApJ 283, 710 (KCb)
Ku W., Kestenbaum H.L., Novick R., Wolf R.S. 1976, ApJL 204, L77
Liedahl D.A., Osterheld A.L., Goldstein W.H. 1995, ApJL 438, L115
Lyne A.G., Graham-Smith F. 1990, Pulsar Astronomy (Cambridge University Press, Cambridge)
Makishima K., Tashiro M., Ebisawa K., Ezawa H., Fukazawa Y., Gunji S., Hirayama M., Idesawa E. et al. 1996, PASJ 48, 171
Mewe R., Gronenschild E.H.B.M., van den Oord G.H.J. 1985, A&AS 62, 197
Morrison R., McCammon D. 1983, ApJ 270, 119
Nomoto K., Tsuruta S. 1987, ApJ 312, 711
Ohashi T., Ebisawa K., Fukazawa Y., Hiyoshi K., Horii M., Ikebe Y., Ikeda H., Inoue H. et al. 1996, PASJ 48, 157
Ögelman H., Finley J.P., Zimmerman H.U. 1993, Nature 361, 136
Pacini F., Salvati M. 1973, ApJ 186, 249
Page D., Applegate J.H. 1992, ApJL 394, L17
Panagia N., Weiler K.W. 1980, A&A 82, 389
Rees M.J., Gunn J.E. 1974, MNRAS 167, 1
Reynolds S.P., Chevalier R.A. 1984, ApJ 278, 630
Reynolds S.P., Chanan G.A. 1984, ApJ 281, 673
Reynolds S.P., Aller H.D. 1985, AJ 90, 2312
Reynolds S.P., Aller H.D. 1988, ApJ 327, 845
Roberts D.A., Goss W.M., Kalberla P.M.W., Herbstmeir U., Schwarz U.J. 1993, A&A 274, 427
Saken J.M., Fesen R.A., Shull J.M. 1992, ApJS 81, 715
Salter C.J., Reynolds S.P., Hogg D.E., Payne J.M., Rhodes P.J. 1989, ApJ 338, 171
Sedov L.I. 1993, Similarity and dimensional methods in mechanics 10th edition (CRC Press, Boca Raton)
Serlemitsos P.J., Jalota L., Soong Y., Kunieda H., Tawara Y., Tsusaka Y., Suzuki H., Sakima Y. et al. 1995, PASJ 47, 105
Seward F.D., Harnden F.R., Helfand D.J. 1984, ApJL 287, L19

Seward F.D., Wang Z.R. 1988, ApJ 332, 199
Slane P. 1994, ApJ 437, 458
Slane P., Lloyd N. 1995, ApJL 452, L115
Slane P., Chen Y., Schulz N.S., Seward F.D., Hughes J.P., Gaensler B.M. 2000, ApJL in press
Tanaka Y., Inoue H., Holt S.S. 1994, PASJ 46, L37
Toor A., Seward F.D. 1974, AJ 79, 995
Torii K., Tsunemi H., Dotani T., Mitsuda K. 1997, ApJL 489, L145
Vasisht G., Aoki T., Dotani T., Kulkarni S.R., Nagase F. 1996, ApJL 456, L59
Vaughan B.A., van der Klis M., Wood K.S., Norris J.P., Hertz P., Michelson P.F., van Paradijs J., Lewin W.H.G. et al. 1994, ApJ 435, 362
Weiler K.W., Panagia N. 1978, A&A 70, 419
Williams D.R.W. 1973, A&A 28, 309
Woltjer L., Salvati M., Pacini F., Bandiera R. 1997, A&A 325, 295
Wu C-C. 1981, ApJ 245, 581
Yancopoulos S., Hamilton T.T., Helfand D.J. 1994, ApJ 429, 832
Zavlin V.E., Pavlov G.G., Shibanov Yu.A. 1996, A&A 315, 141
Zavlin V.E., Pavlov G.G., Trümper J. 1998, A&A 331, 821

Figure captions

Figure 1: Representative energy spectra of the whole SNR obtained by S0C1 and GIS2. The solid lines in the spectra show the best fit power-law model modified by the interstellar absorption. The lower panels show the residuals.

Figure 2: Upper panel shows the upper limits of the emission measure of the thermal component of MEKAL model. Lower panel shows the upper limits of the density for the filling factor of unity (dashed line), and the filling factor of 1/4 (solid line) which corresponds to the Sedov type self similar solution.

Figure 3: Multi-wavelength spectra of the Crab nebula (dashed line) and 3C58. The dotted line shows the extrapolation of the X-ray spectrum.

Figure 4: Photon index of the power-law component as a function of radius with 90% confidence errors. Squares show the case without the blackbody component and the circles show the case with the blackbody component.

Figure 5: Radial profile of the image, the best-fit model function and the PSF as the results of the fitting. Crosses show the data points, circles show the best-fit model function and the triangles show the PSF.

Figure 6: Position of the Gaussian center, x_0 and y_0 in equatorial coordinate (Epoch 2000).

Figure 7: The size of the nebula as a function of the observing energy.

Table 1: Observation date and mode.

Number	Start Time (UT)	End Time (UT)	SIS0	SIS1	GIS2	GIS3
1	14:13 Sep. 12, 1995	07:50 Sep. 13, 1995	C1	C3	PH nominal	PH nominal
2	07:05 Sep. 13, 1995	17:20 Sep. 13, 1995	C0	C2	PH timing	PH timing
3	17:21 Sep. 13, 1995	04:00 Sep. 14, 1995	C2	C0	PH timing	PH timing
4	04:01 Sep. 14, 1995	14:00 Sep. 14, 1995	C1	C3	PH timing	PH timing

Table 2: Effective exposure time [ks].

Number	SIS0	SIS1	GIS2	GIS3
1	22.05	22.19	27.14	27.05
2	12.31	12.31	15.28	15.37
3	15.24	15.34	18.08	18.08
4	13.91	13.93	16.98	16.96

Table 3: Spectral parameters of the whole nebula with the 90% confidence errors. Photon index (γ), normalization ([photons $\cdot$ s^{-1} $\cdot$ keV^{-1} $\cdot$ cm^{-2}] at 1 keV), and the absorbing column density ($n_{\rm H}[10^{21}{\rm cm}^{-2}]$) are summarized.

	S0C1 + S1C3	S0C0 + S1C2	S0C2 + S1C0	G2 + G3
γ	2.24 ± 0.05	2.21 ± 0.08	$2.26\ ^{+0.07}_{-0.06}$	2.32 ± 0.07
Normalization	$(4.9\ ^{+0.3}_{-0.2}) \times 10^{-3}$	$(4.6 \pm 0.4) \times 10^{-3}$	$(4.7 \pm 0.3) \times 10^{-3}$	$(4.7 \pm 0.4) \times 10^{-3}$
$n_{\rm H}$	3.7 ± 0.2	4.0 ± 0.4	4.1 ± 0.3	3.5 ± 0.5
χ^2/d.o.f.	302.1/337	289.2/280	354.1/315	436.3/396

Table 4: 99% confidence upper limits of pulsed fraction in %.

	Energy Range [keV]		
Frequency Range [Hz]	0.7–10	0.7–2	2–10
0.01–1	7	12	11
1–8	10	14	9
8–32	9	19	15
32–64	9	14	12

Table 5: Basic parameters of the Crab nebula and 3C58.

	Crab	3C58
Distance [kpc]	2	3.2
Age [yr] in 1995	941	814
Size [pc] [a]	1.2	2.9×2.2
L_X [ergs s^{-1}] [b]	2.1×10^{37}	2.4×10^{34}
ν_B [Hz] [c]	1×10^{13}	5×10^{10}

Notes. — [a] The size of the nebula at 1 keV defined by the Gaussian FWHM. The value for the Crab nebula is based on Ku et al. (1976).

[b] Total (nebula plus compact source) X-ray luminosity in the energy range 0.5–10 keV. The value for the Crab nebula is based on Toor and Seward (1974).

[c] Frequency of the spectral break. The values are adopted from Green (1994) and the references therein.

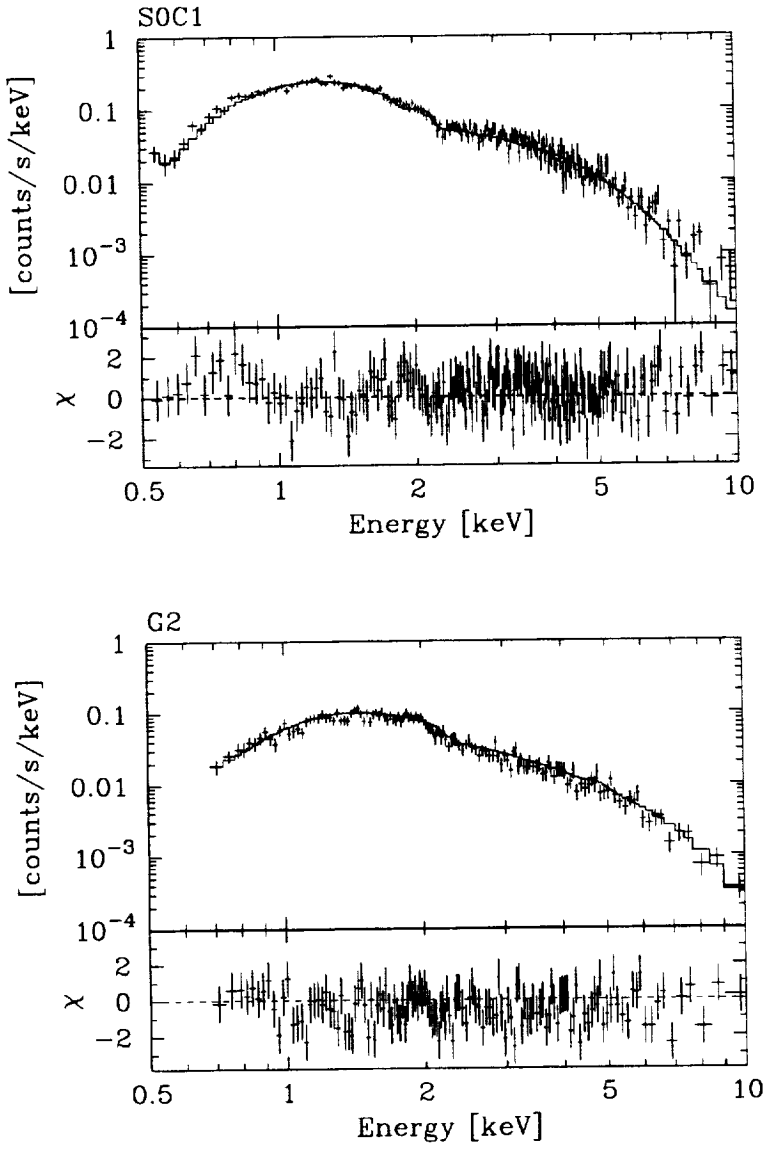
S0C1
[counts/s/keV]
1
0.1
0.01
10^{-3}
10^{-4}
2
0
−2
χ
0.5
1
2
5
10
Energy [keV]
G2
[counts/s/keV]
1
0.1
0.01
10^{-3}
10^{-4}
2
0
−2
χ
0.5
1
2
5
10
Energy [keV]

Figure 1:

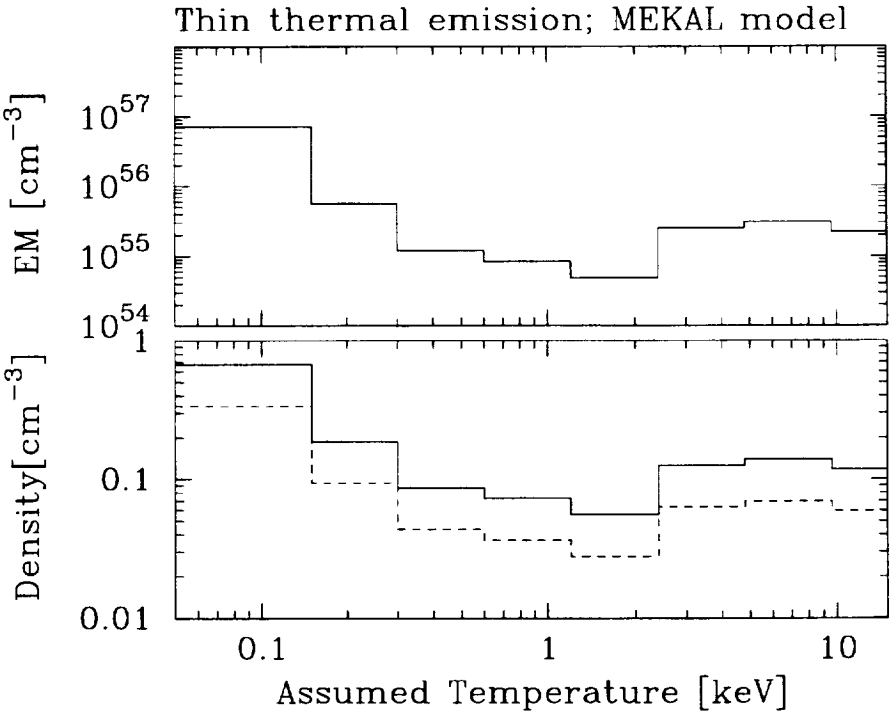
Thin thermal emission; MEKAL model
EM [cm^{-3}]
10^{57}
10^{56}
10^{55}
10^{54}
Density[cm^{-3}]
1
0.1
0.01
0.1
1
10
Assumed Temperature [keV]

Figure 2:

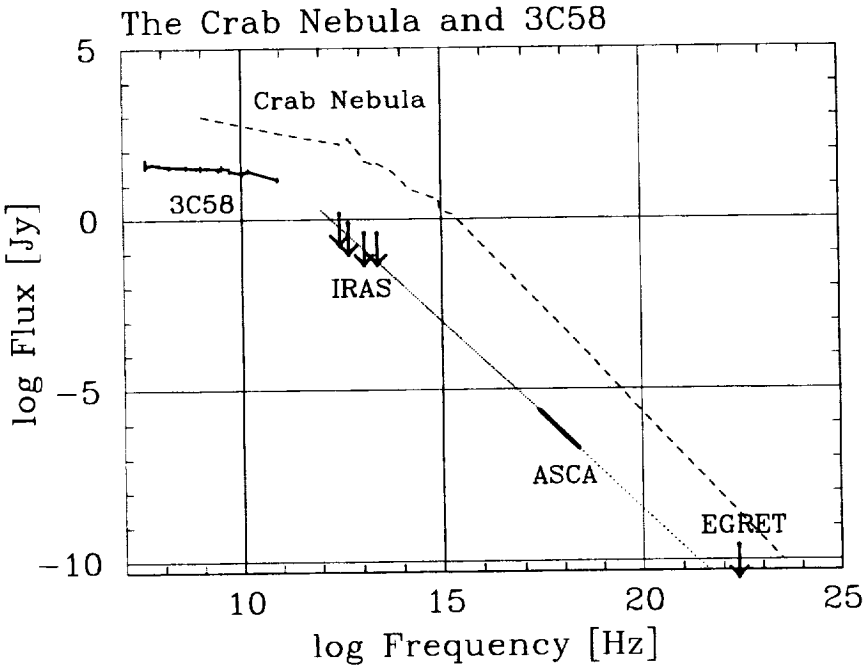
The Crab Nebula and 3C58
Crab Nebula
3C58
IRAS
ASCA
EGRET
log Flux [Jy]
log Frequency [Hz]
5
0
−5
−10
10
15
20
25

Figure 3:

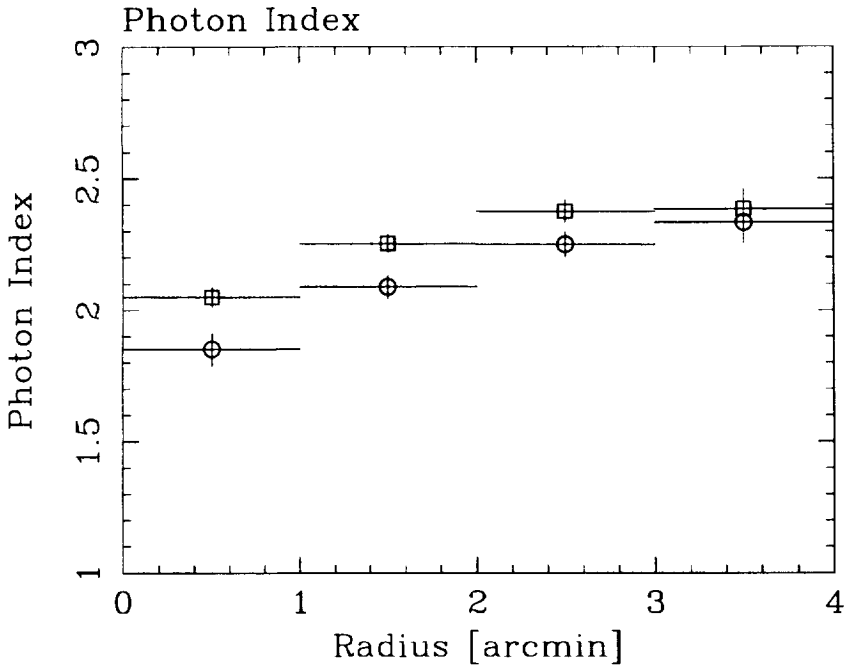

Figure 4:

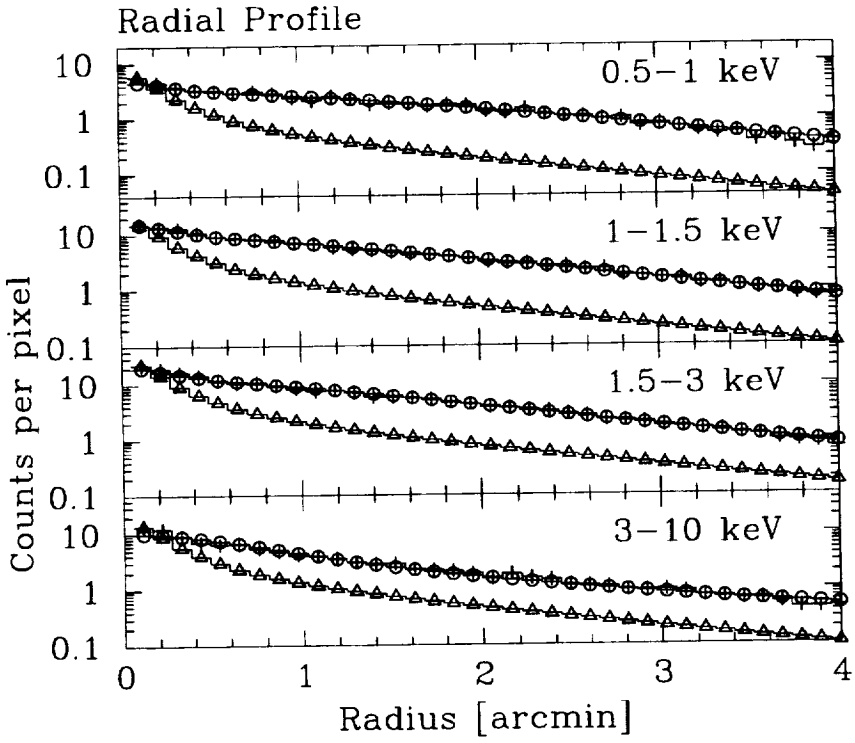
Radial Profile
0.5−1 keV
1−1.5 keV
1.5−3 keV
3−10 keV
Counts per pixel
Radius [arcmin]
10
1
0.1
0
1
2
3
4

Figure 5:

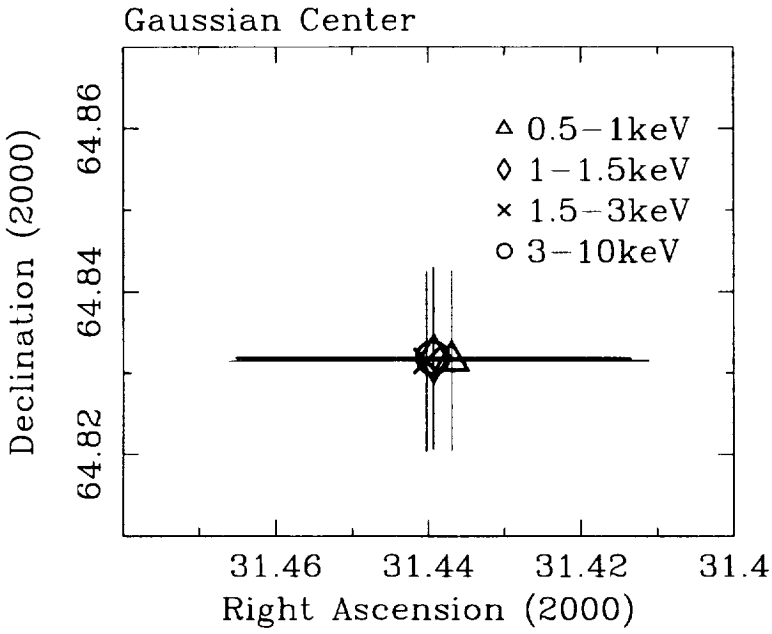
Gaussian Center
Declination (2000)
64.86
64.84
64.82
0.5−1keV
1−1.5keV
1.5−3keV
3−10keV
31.46
31.44
31.42
31.4
Right Ascension (2000)

Figure 6:

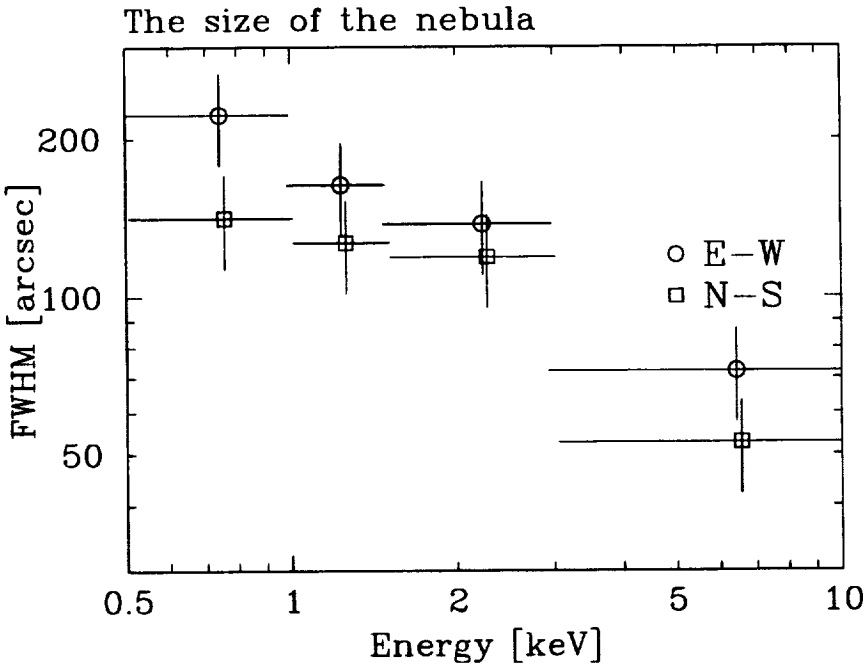
The size of the nebula
FWHM [arcsec]
200
100
50
0.5
1
2
5
10
Energy [keV]
E−W
N−S

Figure 7:

For submission to *The Astrophysical Journal*

A New ASCA and ROSAT Study of the Supernova Remnant: G272.2−3.2

Ilana M. Harrus[1]

NASA/USRA Goddard Space Flight Center, Greenbelt MD 20771

P. O. Slane and R. Smith

Harvard-Smithsonian Center for Astrophysics, Cambridge MA 02138

and

J. P. Hughes

Rutgers University, Piscataway NJ 08854

ABSTRACT

G272.2−3.2 is a supernova remnant (SNR) characterized by an apparent centrally brightened X-ray morphology and thermally dominated X-ray emission. Because of this combination of Sedov-type (thermal emission) and non-Sedov type (non-shell like morphology) features, the remnant is classified as a "thermal composite" SNR. This class of remnant is still poorly understood due in part to the difficulties in modeling accurately all the physical conditions which shape the emission morphology.
In this paper we present a combined analysis of data from the *ASCA* and *ROSAT* satellites coupled with previous results at other wavelengths. We find that the X-ray emission from G272.2−3.2 is best described by a non-equilibrium ionization (NEI) model with a temperature around 0.70 keV, an ionization timescale of 3200 cm^{-3} yr and a relatively high column density ($N_H \sim 10^{22}$ atoms cm^{-2}). We look into the possible explanations for the apparent morphology of G272.2−3.2 using several models (among which both cloud evaporation and thermal conduction models). For each of the models considered we examine all the implications on the evolution of G272.2−3.2.

Subject headings: ISM: abundances – ISM: individual (G272.2−3.2) – shock waves – supernova remnants – X-rays: ISM

---

[1]imh@milkyway.gsfc.nasa.gov

1. Introduction

Supernova remnants are potentially powerful tracers of the complete history of their progenitor star. Their study may provide information not only on the amount of material ejected by the star during the course of its life, but also on the composition of the interstellar medium (ISM) in which the supernova-explosion blast wave propagates.

In a simplified model of supernova evolution, this blast wave propagates through a homogeneous ISM. When the amount of ISM material swept-up by the wave becomes comparable to the mass contribution due to the ejecta, the remnant enters the adiabatic, also called Sedov-Taylor, phase of its evolution (Taylor 1950; Sedov 1959). During this phase, the radiative cooling is negligible and the overall energy of the SNR remains roughly constant. For an SNR evolving according to this model, and in absence of any compact object created during the supernova explosion, the expected X-ray profile is a shell, and its spectrum is characteristic of collisional excitations in a plasma with a temperature around 1 keV. Indeed, a large number of SNRs present this kind of morphology (for example the Cygnus Loop).

However, most of the SNRs do not conform to this simple picture and they present characteristics which substantially differ from this ideal model. One of the many subgroups consists of SNRs which appear centrally bright in X-rays and present spectra dominated by thermal emission. It is widely believed that this peculiar morphology is linked to inhomogeneities in the ISM (one model we use later favors small cold clouds) but few models can account for the measured temperature profiles across remnants in this class. We present here an analysis of recent X-ray observations of G272.2−3.2, including an attempt to reproduce both the morphology and the temperature profile of the remnant. We first examine the existing data on G272.2−3.2, in particular radio and optical observations, and summarize the results obtained from these data. We then describe briefly the X-ray observations used in our analysis. Our image and spectral analysis are presented in § 3, along with a study of the temperature profile and the theoretical modeling of the X-ray morphology. § 4 examines the consequences of the results presented in the previous paragraph. There we discuss and summarize the main points of the paper.

2. From Radio to X-Ray: Pre-*ASCA* knowledge on G272.2−3.2

G272.2−3.2 was discovered in the *ROSAT* All-Sky Survey (Greiner and Egger 1993). It presents a centrally filled X-ray morphology and a thermally dominated X-ray spectrum. The temperature, as determined by the *ROSAT* PSPC observation is relatively high (between 1.0 and 1.5 keV for a 1σ confidence level). No significant variation of the temperature could be measured with the X-ray data available from the *ROSAT* PSPC (Greiner, Egger, and Aschenbach 1994).

Optical observations (Winkler and Hanson 1993), made soon after the announcement of the discovery, confirm the nature of the nebulosity as a supernova remnant and the shock-heated nature of the emission. In particular, both the measured [SII]/Hα ratio and the detected emission from [NII] 658.3-nm and [OII] 732.5-nm are typical of SNRs. One of the fainter filaments is located at

$09^h06^m40^s.4$, -52°06′42″ (J2000), about 1′ north-west of the X-ray emission center. Brighter filaments with a similar [SII]/Hα are detected at $09^h06^m12^s.4$, -52°06′52″. There is no evidence for diffuse emission in the continuum images of the field.

Detailed radio observations (Duncan et al. 1997) have introduced a wealth of new data about this SNR. The radio observations were conducted at multiple frequencies and baselines using the Parkes radio telescope, the Australia Telescope Compact Array (ATCA) and the Molonglo Observatory Synthesis Telescope (*MOST*). G272.2−3.2 is of such low surface brightness ($\sim$ 1 mJy at 843 MHz) that even the sub-arcminute *MOST* observations could only map the brightest parts of the remnant. G272.2−3.2 presents an incoherent filamentary structure with diffuse, non-thermal emission of very low surface brightness as well as bright "blobs" which correlate well with the brightest optical filaments. This is a good indication that optical and radio emission emanate from the same regions. These regions are likely to be the ones where the shock interaction with the ISM is the strongest. We show in Fig. 1 a *MOST* radio image extracted from Duncan et al. (1997) on which the authors show the position of the optical filaments. There is no evidence for a clean "shell-like" morphology although the remnant is roughly circular with a 20′ diameter and has a steep non-thermal radio spectral index (0.55±0.15), which is more typical of shell-like remnants than plerions. This implies that the diffuse emission detected within G272.2−3.2 is most probably due to shock-accelerated electrons. The spectral index varies relatively little across the remnant. There is no evidence of polarized emission from the remnant and Duncan et al. (1997) argue that this depolarization may be the result of turbulence occurring on angular scales of the order of 1′. There is no evidence of pulsar-driven nebula.

There are data from the Infrared Astronomical Satellite (*IRAS*) survey at 12, 25, 60 and 100 μm. Infrared observations are unique in that they provide direct information on the dust present in the ISM and so they can serve as a powerful tool for temperature diagnostics. We have extracted the *IRAS* data[1] at all four wavelengths and present our findings in the next section.

There are CO maps of the G272.2−3.2 sky region at a resolution of 18′ (larger than the remnant). In this direction in the sky, velocity changes very little along the line of sight adding to the difficulty of constraining the distance to the remnant. The only significant CO emission is measured at velocities between -20 km s^{-1} and 20 km s^{-1} (T. Dame - private communication).

At a distance greater than 2 kpc, the large galactic latitude of G272.2−3.2 implies a distance below the plane larger than 110 pc. Using the distance distribution of SNRs in the Galaxy (Mihalas and Binney 1981) and their galactic latitude (Green 1998), we estimate that less than 10% of galactic SNRs are located at a greater distance from the plane. This results is in agreement with 100 pc upper limit given by Allen (1985) for the distance distribution of stars above the plane of the Galaxy and suggests a distance of about 2 kpc to G272.2−3.2.

This estimate, although solely based on a statistical analysis, turns out to be in good agreement with a value of $1.8^{+1.4}_{-0.8}$ kpc based on the measured X-ray column density of $N_{\rm H} = 4.6\pm3\times10^{21}$ atoms cm^{-2} (Greiner, Egger, and Aschenbach 1994). We also derive an estimate of an upper limit for the dis-

[1]Data extracted from the HEASARC-SkyView site at: http://skyview.gsfc.nasa.gov/

tance to the remnant. Using stars within a distance of 2 kpc, Lucke (1978) finds an optical color excess with distance of roughly 0.2 mag kpc^{-1} in the direction of G272.2−3.2. Using the relation between color excess and column density ($N_H = 5.9 \times 10^{21} \times E_{B-V}$ atoms cm^{-2}) of Predehl and Schmitt (1995), one gets an upper limit of about 10 kpc for the distance to G272.2−3.2.
In view of all the uncertainties on the distance measurement, we adopt an "intermediate" distance scale of 5 kpc in the following computation and will examine the consequences of this estimate on the different dynamical states of the remnant. One must keep in mind that this value is mainly used as a scaling factor; we will keep the distance variation explicit in all our computations to allow easy computations at other distances of the physical quantities derived.

3. *ASCA* observations

3.1. Spatial Analysis

3.1.1. Images

ASCA carried out one observation of G272.2−3.2 on 1995 January 20 at a nominal pointing direction of $09^h06^m43^s.2$, -52°06′14″.4 (J2000). After applying the standard cuts on the data, we generated exposure-corrected, background-subtracted merged images of the GIS and SIS data in selected spectral bands. Background was determined from the weighted average of several nominally blank fields from high-galactic latitude observations with data selection criteria matched to those used for the SNR data. Exposure maps were generated from the off-axis effective-area calibrations, weighted by the appropriate observation time. Events from regions of the merged exposure map with less than 10% of the maximum exposure were ignored. Merged images of the source data, background, and exposure were smoothed with a Gaussian of $\sigma = 30''$ for both the low-energy band (0.5–4.0 keV) and the high-energy band (4.0–10.0 keV). We subtracted smoothed background maps from the data maps and divided by the corresponding exposure map. Fig. 2 shows the results obtained for the two detectors in the low energy band. The SNR is not detected above 4.0 keV and confirms the result from radio data that there is no sign of a pulsar-driven nebula. To examine the morphology of the remnant in more detail, we have generated SIS images in narrow energy bands in an attempt to isolate contributions from separate elements. We have minimized the continuum component by subtracting the average contribution from a small range of energy around each line imaged. In Fig. 3 we show SIS images of G272.2−3.2 in the three narrow energy bands [1.20 keV–1.35 keV], [1.70 keV–1.90 keV] and [2.25 keV–2.50 keV] corresponding to Mg XI, Si XIII, S XV lines respectively. The minimum visible in the center of all the images is due to an instrumental effect and corresponds to the location of the wide gap between CCDs in the SIS detector. There is a strong correlation between the Mg XI energy band map and the broad energy image. In the next section (spectral analysis) we will examine how this effect translates to a higher value of magnesium abundance inside the region of maximum emission.

3.1.2. Comparison with existing data

To get yet a better estimate of the morphology of this remnant, we have analyzed *ROSAT* data from both the High Resolution Imager (HRI) and the Position Sensitive Proportional Counter (PSPC). Both sets of data were cleaned according to the standard prescription to study extended sources (Snowden et al. 1994). The software[1] computes the contributions from the different backgrounds (solar scattered X-rays, high-energy particles, long and short term enhancements) and subtracts them from the data. Similar corrections are made for the HRI although contamination from those backgrounds is known with less accuracy. Fig. 4 shows the result of this procedure for the *ROSAT* HRI (the result is similar for the PSPC). A bright spot at the western edge of G272.2−3.2 is seen with a flattening of the shell at this location which coincides with the bright optical filament detected by Winkler and Hanson (1993). One explanation for this bright spot is that the expanding shock is encountering a density gradient in the local ISM. It could also well be that the shock has engulfed a cloud, slowed down, and that the cloud is being evaporated. At a distance of 5 kpc, the angular size of about 2′25″ implies a cloud 3.5 pc in size. Using the results from the spectral analysis (see next section) we deduce a density between 0.42 and 0.70 cm^{-3} for the clouds. The soft emission of that region is compatible with both explanations.

One useful indicator of the presence of dust in the galaxy is in the infrared energy band. Using data from the *IRAS* survey, Saken, Fesen and Shull (1992) studied the infrared emission from 161 galactic SNRs. They argue that young remnants tend to have strongest fluxes at 12μm and 25μm while somewhat older remnants have their strongest emission at longer wavelengths. G272.2−3.2 was not part of this study although its *IRAS* data show strong emission at 60 and 100μm (15 and 70 MJy str^{-1} respectively) probably associated with the shock heated dust in the ISM. There is no significant emission at the two smallest wavelengths, a possible indication of a low dust temperature. One of the techniques commonly used to distinguish legitimate SNR emission from HII regions and eliminate potential calibration or normalization problems, consists of studying the ratio of maps (60μm/100μm; 12μm/25μm) as an indicator of the respective contributions. This technique, applied with success for the Cygnus Loop (Saken, Fesen and Shull 1992) has the advantage of being both simple and free from a lot of theoretical assumptions (about grain emissivities for example) that would otherwise complicate the interpretation.

We computed the ratio F_{60}/F_{100} from the remnant (using the X-ray image to define its extent). We find that $F_{60}/F_{100} \sim 0.2$ which is comparable with what was measured for Vela XYZ (Saken, Fesen and Shull 1992) but still lower than almost all the other ratios quoted (the highest being 2.45 for Kepler's SNR). This low value of the F_{60}/F_{100} emission is consistent with the low dust temperature hinted by the lack of emission at 12μm and 25μm. Fig. 5 shows the smoothed (with a Gaussian of 3′) image of the 60μm/100μm ratio and contours from a close-up of this image shown with the *ROSAT* HRI image superposed. The correlation with the brightest part of the SNR (the western part of the remnant) is obvious and in complete agreement with the optical, radio and X-ray data.

[1]Available via anonymous ftp at "legacy.gsfc.nasa.gov".

It is remarkable not only that the SNR is so obviously detected in the *IRAS* data (and its very high background level), but that the agreement with the HRI image is so good. In the next section, we analyze spectra extracted from the brightest region and the rest of the remnant. The results from both spectral and spatial analysis are then used to form the global picture of the remnant.

3.2. Spectral Analysis

Depending on the age of G272.2−3.2 and on the pre-shock medium density, non-equilibrium ionization effects can become important (Itoh 1979). In this case, a simple equilibrium collisional plasma emission model (Raymond & Smith 1977 - CEI model) can no longer be applied to reproduce the expected X-ray spectra. One has to take into account the fact that the ions are not instantaneously ionized to their equilibrium configuration at the temperature of the shock front. This model has, in addition to the temperature, an additional parameter which describes the state of the plasma ionization. This ionization state depends on the product of electron density and age and we define the ionization timescale as $\tau_i \equiv n_e t$. We have used an NEI model (Hughes and Helfand 1985) keeping all the elemental abundances at their value given in Anders and Grevesse (1989) except when explicitly mentioned. In order to check the possibility of weak non-equilibrium ionization effects (for the dynamically older parts of the remnant), we have run both models (CEI and NEI) and compared the results from our spectral analysis.

3.2.1. Results from the Spectral Analysis

We have carried out several spectral analyses using the different data sets available and then combined them in order to obtain a general picture of the remnant. We have already seen that the remnant is undetected above 4 keV; all channels above that energy are ignored in the following analysis. After a first fit using only the *ASCA* data, we added data from the *ROSAT* PSPC to constrain $N_{\rm H}$, the value of absorption along the line of sight, using the cross-sections and abundances from Morrison & McCammon (1983). In all the analyses, the data were extracted from the *ROSAT* PSPC observation and then spatially matched to that of *ASCA*. We added a gain shift to both GIS 2 and GIS 3 (the same value for both detectors) according to the prescriptions from the calibration data analysis done by the *ASCA*-GIS team[1]. An initial *ASCA* analysis was done on the complete remnant. We extracted a total of 25000 GIS events from a circular region encompassing the total emission region. The SIS was not used for the full SNR spectrum because the remnant covers more than one chip. We found that although it was impossible to describe accurately the complete SNR using a single model (CEI or NEI), the quality of the fit improves dramatically (from a χ^2 of 870 to 514, for 325 degrees of freedom) in going from a CEI to an NEI model. We found a common gain shift (for both GIS 2 and 3) of -3.3% , consistent with the results found by the GIS

[1]see http://heasarc.gsfc.nasa.gov/docs/frames/asca_proc.html for more informations on calibration issues.

calibration team.
The spectrum shown in Fig. 6 shows strong residuals at the silicon and sulfur energy lines. Neither the NEI nor the CEI can accurately model these two strong emission features.
In the next step of the analysis, we included data from the *ROSAT* PSPC data in the fit. In this case the column density is $N_{\rm H} = 1.12 \pm 0.02 \times 10^{22}$ atoms cm^{-2}, the ionization timescale is 2150^{+320}_{-360} cm^{-3} years, while the temperature is $kT = 0.73^{+0.03}_{-0.04}$ keV (associated with a χ^2/ν of 691.95/354). Both ionization timescale and the temperature of the plasma are compatible with the results found in the previous analysis but the column density is smaller. The total unabsorbed flux between 0.2 and 3.0 keV is $2.35 \pm 0.15 \times 10^{-10}$ ergs cm^{-2} s^{-1}. The fit for the complete remnant is shown in Fig. 6 and all the results are given in Table. 1. We note that the errors quoted for the measured parameters are underestimates in that they correspond to a fit with a large χ^2/ν.
In order to get a more quantitative picture of the remnant, we have separated it into "A" and "B", two non-overlapping regions of emission. The "A" region is chosen to encompass the bright western part of the remnant (see Fig. 2 –left panel– or the following paragraph for a definition of the region) while the "B" spot is taken from the other region of the SNR, where no optical filaments have been observed.

3.2.2. Study of the "A" Region

We have extracted events from the "A" region defined in the *ROSAT* PSPC as a ~ 2 'radius circle centered at $09^{\rm h}06^{\rm m}11^{\rm s}.4$, -52°05′34″.4 (J2000).
The same region is then selected for the *ASCA* SIS and GIS. Unfortunately the region is at the edge of the *ASCA* SIS and the circular region of extraction is truncated to take this into account. After background subtraction, the count rate is 0.084 ± 0.002 cts s^{-1}, 0.024 ± 0.001 cts s^{-1}, and 0.017 ± 0.001 cts s^{-1} in the *ROSAT* PSPC and *ASCA* SIS/GIS respectively (we have averaged the values for SIS 0 and SIS 1 as well as those for GIS 2 and GIS 3).
We model the five spectra using the NEI model mentioned above. As previously a gain shift is included in the analysis of GIS 2 and GIS 3 data.
The resulting χ^2/ν is 248.35/133. All the results for region "A" are consistent with the ones found for the complete remnant when fit with a NEI thermal model. We find a column density of $N_{\rm H} = 1.17^{+0.02}_{-0.06} \times 10^{22}$ atoms cm^{-2}, an ionization timescale of 760^{+830}_{-70} cm^{-3} years and a temperature of $kT = 0.86^{+0.08}_{-0.22}$ keV. We found a gain shift of -3% consistent with the results found previously (see results Table. 2a.). In comparison a fit using a CEI model (Mewe, Gronenschild and van den Oord 1985; Mewe, Lemen and van den Oord 1986; Kaastra 1992), leads to a worse fit ($\chi^2_{\rm r} = 1.96$).
As we defined region "A" to be coincidental with the region of enhanced Mg X lines (see circle in Fig. 3), we added magnesium abundance as an extra parameter in the fit and check for any statistically significant drop in χ^2. With this one extra parameter, the χ^2/ν is now 176.07/129. The probability to exceed this value per chance is 0.003 compared to 5×10^{-9} for the previous fit. The column density is consistent with the previous result ($N_{\rm H} = 9.5^{+0.7}_{-1.0} \times 10^{21}$ atoms cm^{-2}), and so are the temperature ($kT = 1.00^{+0.35}_{-0.08}$ keV) and the ionization timescale (1385^{+1860}_{-550} cm^{-3} years).

The SIS detectors (the more sensitive instruments for measuring any abundance variation) do show a departure from the cosmic value (the smallest acceptable values range between 1.3 to 2 times solar abundance) but one has to keep in mind that the data were taken in a 4-CCD mode with degraded resolution and non-optimized calibration. All the other detectors yield spectra indistinguishable from models with cosmic values; the energy resolution of the *ROSAT* PSPC is too low to be sensitive to abundance variations, and both GIS spectra do show small indication of enhanced magnesium abundances, but the large χ^2 resulting from the strong residuals at silicon and sulfur line energies renders it difficult to assess its significance (results are given in Table. 2b.).

3.2.3. Study of the "B" Region

We have carried out an identical analysis on the "B" region which, as mentioned above, designates the part of the remnant located at the other "edge" of G272.2−3.2. We extracted data from an ellipse of 2′41″ and 5′35″ minor and major axis, and located at $09^h07^m14^s.5$, -52°06′19″.6 (J2000) (see Fig .3 - left panel).

This region selection allows us to study most of the emission within the remnant, but encompasses more than one CCD on the SIS detectors. The data from these detectors had to be combined prior to any analysis. As in the previous analysis, we used data from the *ROSAT* PSPC to constrain the value for the column density. After background subtraction, the count rates are 0.19 ± 0.003 cts s^{-1} for the *ROSAT* PSPC and 0.075 ± 0.001 cts s^{-1}, and 0.066 ± 0.001 cts s^{-1} in *ASCA* SIS and GIS respectively.

We fit the data sets using an NEI model. Only the normalization varies from data set to data set. We applied a gain shift equal to that found in the previous analysis. We find (χ^2/ν= 635/317) a column density of $N_{\rm H} = 1.30^{+0.03}_{-0.04} \times 10^{22}$ atoms cm^{-2}, associated with a temperature of $kT = 0.65^{+0.06}_{-0.02}$ keV and an ionization timescale of $4180^{+960}_{-1290} cm^{-3}$ years (see Table. 3. for a summary).

From all the previous analysis, it seems possible to get a consistent description of the remnant. Both regions "A" and "B" have compatible temperature and ionization timescale. In the following section, we will examine what picture of the evolutionary state of the remnant these results imply.

3.3. Radial Temperature Gradient

One of the important goals of this work is to understand the origin of the centrally-peaked X-ray morphology of the remnant. The temperature profile is an important diagnostic tool to separate between models which can explain this kind of morphology. Some models, like a one-dimensional, spherically symmetric, hydrodynamic shock code (Hughes, Helfand, and Kahn 1984), predict measurable variations of the observed temperature across the remnant, while others do not (White & Long 1991; hereafter WL). We have studied temperature variations across the remnant using data from the GIS 2. The remnant was separated in 5 annuli centered at $09^h06^m46^s$, -52°06′36″.14 (J2000) chosen so as to contain the same number of events (around 3220 events) per annulus. We

fixed the column density and the ionization timescale to the values found in the previous spectral analysis. All elemental abundances are kept linked to each other at their nominal ratio. This is only an approximation used to get an estimate of the possible temperature variation across the SNR. In the following section, we will examine both the temperature and surface brightness profile and consider two scenarios (evaporation of cold clouds in the remnant interior and late-phase evolution incorporating the effects of thermal conduction) which have been applied to other remnants successfully to reproduce both the morphology and the temperature profile.

3.4. Radial profile of G272.2−3.2

3.4.1. Sedov-Taylor solution

In the soft X-ray band G272.2−3.2 is almost perfectly circular in appearance with a radius of $8'$. As mentioned in the §2, the distance to G272.2−3.2 is not well known and its measured column density is large. In addition, there is no trace of any high-energy contribution from a central object. In this context, we have examined the possibility that G272.2−3.2 is a standard shell-like remnant which appears centrally peaked because of the large absorption along the line of sight or because of projection effects. If there were a density enhancement in the shell near the projected center of the remnant (due for example to the possible presence of metal-rich ejecta) that was similar to the density enhancement at the location of the shell toward the west, the remnant would have a centrally peaked morphology similar to the one observed. The fact that G272.2−3.2 presents both some limb brightening and centrally peaked emission could support this simple explanation. To quantify this model a little bit more we have studied the profile of G272.2−3.2 in the *ROSAT* HRI in 4 different quadrants of the remnant. We chose the quadrants so that the brightest part of the remnant (that we called region "A" in our spectral analysis) belongs to one quadrant only. The profiles are shown in Fig. 7 and reveals the distinct enhancement on the west-side of the remnant. We have computed then the expected X-ray emission in the center for a simple shell model in which the inner radius is taken at 5 $'$(instead of the 7.4 $'$expected in the standard Sedov-Taylor solutions) to accommodate the measured west enhancement. We find that the central X-ray emission enhancement in the northern quadrant is a factor of 3 to 4 times brighter than expected from the shell at that position. This requires a density about a factor of two higher than in the shell, a factor not excluded by our analysis. In this case, the remnant evolution can simply be described by a set of Sedov-Taylor self-similar solutions.

The total X-ray emitting volume is $V = 1.94 \times 10^{59}\, f\, D_5^3\, \theta_8^3$ cm^3, where f is the volume filling factor of the emitting gas within the SNR, D_5 is the distance to the remnant in units of 5 kpc, and θ_8 the angular radius in units of $8'$. In the following discussion, we have used the results of the NEI fit to the complete remnant (*ASCA* GIS and *ROSAT*-PSPC combined; see Table. 1.). Because of the relatively large value of the χ^2 found in our best fit analysis, we have estimated physical parameters using a larger range of values than that found by the standard χ^2 analysis and given in Table. 1 (we increased the errors by a factor 3). For an NEI normalization ranging from 3.2 to

4.1×10^{12} cm^{-5} and a ratio $n_e/n_{\rm H}$ between 1.039 and 1.084, we get a hydrogen number density $n_{\rm H}$ between 0.21 and 0.25 $D_5^{-1/2}\,\theta_8^{-3/2}\,f^{-1/2}$ cm^{-3}. The mass of X-ray emitting plasma M_X, in a Sedov-Taylor model, is between 35 and 184 $D_5^{5/2}\,f^{1/2}\theta_8^{3/2}\,M_\odot$. The estimated age of the remnant varies between 6250 and 15250 years and the initial supernova explosion ranges between 1.3 and 4.9 $\times 10^{50}\,D_5^{5/2}\,\theta_8^{3/2}\,f^{-1/2}$ ergs. At a distance of 2 kpc (our lower limit on the distance), the emitting X-ray mass value is too small to allow for the remnant to have reached its Sedov-Taylor phase and the energy explosion is quite atypical of a supernova event.

As indicated in all the quantities derived, all these estimates have a strong dependence on the distance to the remnant. If the remnant is even further away than the distance derived by Greiner, Egger, and Aschenbach (1994), and this may well be the case, considering that the distance estimate used there is probably inaccurate by at least a factor 2, it is not impossible to reconcile the values deduced for both the emitting X-ray mass and the initial explosion energy with acceptable estimates for a standard SNR.

3.4.2. Cloudy ISM

Although it is possible that the centrally peaked X-ray morphology of G272.2−3.2 is due to the viewing effects mentioned in the previous section, we have examined other scenarios which could also explain it. In particular we have used a model (White and Long 1991) based on cloud evaporation. This model invokes a multi-phase interstellar medium consisting of cool dense clouds embedded in a tenuous intercloud medium. The blast wave from the SN explosion propagates rapidly through the intercloud medium, engulfing the clouds in the process. In the model, these clouds are destroyed by gradually evaporating on a timescale set by the saturated conduction heating rate from the hot post-shock gas. Since this timescale can be long, it may be possible for cold clouds to survive until they are well behind the blast wave which, as they evaporate, can significantly enhance the X-ray emission from near the center of the remnant.

The timescale for cloud evaporation is one of the two extra parameters in the WL model added to the three of the standard Sedov solution: explosion energy E_0, ISM density n, and SNR age t. This timescale, which is expressed as a ratio of the evaporation timescale to the SNR age, $\tau_e \equiv t_{\rm evap}/t$, nominally depends on different factors, such as the composition of the clumps and the temperature behind the shock front, although such dependencies are not included explicitly in the model. The other extra parameter, C, represents the ratio of the mass in clouds to the mass in intercloud material. For appropriate choices of these parameters, the model can reproduce a centrally peaked X-ray emission morphology - see for example the application of this model to the centrally-peaked remnants W28 and 3C400.2 (Long et al. 1991). In the evaporating model atoms from the cold clouds enter the hot medium on timescales smaller than the ionization timescale. The line emission occurs after the ion has left the cloud and the ionization occurs in the hot phase. In this case, one would expect the highest ionized material to be near the center of the remnant or equivalently, to have the smallest range of ionization timescales further out. In all the following analysis, we have used emissivities derived from the NEI model with the ionization timescale fixed to the value of

the complete remnant analysis.
We explored the parameter space of the two extra parameters and compare in Fig. 8 the results found for 3 representative sets of parameters with the HRI profile deduced for both the northern and western quadrants (as defined in Fig. 7). We also compared the expected temperature profile for the best value of C and τ with the *ASCA* GIS measured temperature profile using an NEI model as described in Section 3.3. One can see that we can reproduce the emission weighted temperature variation across the remnant. The predicted profile agrees within the error bars with the emission profile from the most "centrally peaked" quadrant of the remnant but disagree with the profile extracted from the Western part of G272.2−3.2 (shown in dotted lines on Fig. 8). For comparison we have kept two other good trials for (C, τ) equal to (50,20) and (35,10) respectively. The WL model allows for variations from the Sedov-Taylor in the physical quantities estimated from the spectral analysis but the differences stay small. For the values of (C=100,τ=33) which provide an acceptable fit to the data, M_X does not vary by more than 10% from the value derived in the Sedov-Taylor model.

3.4.3. Thermal conduction model

Thermal conduction is an alternative model to explain the morphology and emission from thermal composite remnants, and was used most notably for the SNR W44 [see Cox et al. (1999) for a detailed description of the model, and Shelton et al. (1999) for its application to W44]. It can be summarized as the first attempt to include classical thermal conduction in a fully-ionized plasma (Spitzer 1956), moderated by saturation effects (Cowie and Mckee 1977), to smooth the large temperature variations that are created in a Sedov-Taylor explosion. The result is a very flat temperature profile, dropping rapidly at the edge of the remnant.
We used ODIN, a one-dimensional hydrocode which includes the effects of non-equilibrium cooling and thermal conduction (Smith and Cox 2000) to create models for a grid of explosion energies, ambient densities, and ages. SN explosion energies from $0.3 - 2 \times 10^{51}$ ergs were considered along with ambient densities from 0.05-10 cm^{-3}, for ages in the range 2000-50,000 years. These give a range of remnant radii, X-ray spectra, and surface brightnesses that can be compared to the observed values for the remnant. As shown in Fig. 8, the best-fit temperature varies between 0.65-0.8 keV, and the surface brightness from $0.5 - 2.5 \times 10^{-3}$ cts s^{-1} arcmin^{-2} in the *ASCA* GIS. The average surface brightness is $\sim 10^{-3}$ cts s^{-1} arcmin^{-2}.
We found that low ($n_0 \lesssim 0.5\,\mathrm{cm}^{-3}$) ambient densities were required in order to get a central temperature of 0.7 keV, just as was found in the Sedov-Taylor model. Higher densities led to lower temperatures (assuming a fixed surface brightness of 10^{-3} cts s^{-1} arcmin^{-2}), independent of the explosion energy. All other SNRs where the thermal composite model has been used successfully showed much higher ambient densities [4.72 cm^{-3} for W44 (Shelton et al. 1999) and a best-fit density between 1-2 cm^{-3} for MSH 11−61*A* (Slane et al. 2000)]. This low inferred density is a direct result of the high measured temperature, substantially larger than in those SNRs. In addition, the radial extent of the remnant on the sky is 8′, so the physical radius is $11.6 D_5$ pc. The thermal

conduction models we examined with the observed surface brightness and temperature require a minimum radius of 13.5 pc and age of 12,000 yr, suggesting a minimum distance of 5.8 kpc in the case of an explosion energy of 3×10^{50} ergs. A larger explosion energy will increase the radius and therefore the distance estimate.

We compared the observed GIS spectrum against solar-abundance NEI models from ODIN and the Raymond-Smith (Raymond and Smith 1977) plasma model. Using the above-mentioned explosion parameters, the Sedov-Taylor swept-up mass is $\approx 120 M_{\odot}$. The spectrum derived in this configuration leads to a reduced χ^2 of 5.7 (assuming a column density of 1.3×10^{22} atoms cm^{-2}). In addition, while the model matches the He-like magnesium lines at 1.4 keV, the model silicon emission at 1.8 keV is less than half the observed value, and the sulfur lines at 2.46 keV are far too weak. Using larger explosion energies only increases this trend in the models. This suggests that either the SNe that formed G272.2−3.2 had an atypically-small explosion energy, or that a thermal-conduction SNR model which does not include ejecta is not a good fit to the observations.

4. Discussion & Summary

G272.2−3.2 presents a couple of puzzles that we have addressed in this paper. First, the X-ray data point to a youngish remnant (its size – at the assumed distance of 5 kpc, its X-ray temperature, and the potential overabundance of Mg, Si and S) although its infrared emission resembles an older remnant profile. This lack of 12 μm and 25 μm emission could be due to a low dust density possible if the supernova explosion occurred in a cavity. Such a scenario would imply a massive progenitor (more than 8 to 10 $M_{\odot}$) with strong stellar winds, but is hard to combine with the model of a cloudy ISM put forward to explain the morphology. Note that according to nucleosynthesis models, a progenitor more massive than $15 M_{\odot}$ would yield more than 0.046, 0.071, and 0.023 $M_{\odot}$ of Mg, Si and S respectively (Thielemann, Nomoto and Hashimoto 1996), which would require a swept-up mass of more than $100 M_{\odot}$ to lead to Mg and Si abundances less than twice that of cosmic abundances.

The radio morphology of G272.2−3.2 is difficult to characterize simply because of its low surface brightness which prevented a complete mapping of the remnant by the ACTA.

The X-ray peaked morphology can be explained by viewing effects or a cloud evaporation model. Both explanations provide reasonable estimates for the initial explosion energy and the total mass swept-up (depending here again on the distance estimate). A model involving thermal conduction, successfully applied to W44 (Shelton et al. 1999) requires the remnant to be around 5000 years old and associated with a low SN explosion energy. The model fails to reproduce the centrally peaked morphology of the remnant, consistent with G272.2−3.2 being too young for thermal conduction to have taken place.

The spectrum of the entire remnant presents evidence of strong lines (in the residuals of the *ASCA* GIS) which are not easily accounted for in the existing models (both CEI and NEI models). This could be a result of a a degraded response of the detectors, bad determination of the gain applied to the signal or the sign of something more fundamental, linked either to the simple models used

or the properties of the remnant itself. We note that such strong lines are detected at the same energy range in at least two other remnants which present similar morphological characteristics: W44 (Harrus et al. 1997) and MSH 11−61*A* (Slane et al. 2000).
Because of the distance uncertainty, it is difficult to derive the initial parameters of the remnant (time and initial energy of the explosion). Low explosion energy supernovae do occur (see Mazzali et al. 1994 and Turatto et al. 1996 for the study of SN 1991bg) but this would be hard to reconcile with a massive progenitor scenario.
All these estimates are consistent with G272.2−3.2 being in the adiabatic phase of its expansion, but depend crucially upon the distance to the remnant. A better determination of this parameter would help characterize unambiguously the evolutionary state of G272.2−3.2 and will help further constrain the general picture of SNR's evolution.

Our research made use of data obtained from the High Energy Astrophysics Science Archive Research Center Online Service, provided by the NASA/Goddard Space Flight Center. POS acknowledges support through NASA grants NAG5-2638 and NAG5-3486, and contract NAS8-39073.

REFERENCES

Allen, C. W. 1985, Astrophysical Quantities, The Athlone Press, London

Anders, E., & Grevesse, N. 1989, Geochimica et Cosmochimica Acta, 53, 197

Cowie, L. L. & McKee, C. F. 1977, ApJ,211, 135

Cox, D. P., Shelton, R. L., Maciejewski, W., Smith, R. K., Plewa, T., Pawl, A., and Rozyczka, M. 1999, ApJ, 524, 179

Duncan, A. R., Primas, F., Rebull, L. M., Boesgaard, A. M., Deliyannis, C. P., Hobbs, L. M., King, J. R., and Ryan, S. G. 1997, MNRAS, 289, 97

Green, D. A. 1998, 'A Catalogue of Galactic Supernova Remnants (1998 September version)', Mullard Radio Astronomy Observatory, Cambridge, United Kingdom (available on the World-Wide-Web at "http://www.mrao.cam.ac.uk/surveys/snrs/")

Greiner, J. & Egger, R. 1993, IAU Circ No 5709

Greiner, J., Egger, R., & Aschenbach, B. 1994, A & A, 286, L35

Harrus, I. M., Hughes, J. P., Singh, K. P., Koyama, K., & Asaoka, I. 1997, ApJ, 488, 781

Hughes, J. P., Helfand, D. J., & Kahn, S. M. 1984, ApJ, 281, L25

Hughes, J. P. & Helfand, D. J., 1985, ApJ, 291, 544

Itoh, H. 1979, PASJ, 31, 541

Kaastra, J. S. 1992, An X-Ray Spectral Code for Optically Thin Plasmas, Internal SRON-Leiden Report, updated version 2.0

Long, K. S., Blair, W. P., Matsui, Y., & White, R. L. 1991, ApJ, 373, 567L

Lucke, P. B. 1978, A&AS, 64, 367

Mazzali, P. A., Chugai, N., Turatto, M., Lucy, L. B., Danziger, I. J., Cappellaro, E., della Valle, M., and Benetti, S. 1997, MNRAS, 284, 151

Mewe, R., Gronenschild, E. H. B. M., & van den Oord, G. H. J. 1985, A&AS, 62, 197

Mewe, R., Lemen, J. R., & van den Oord, G. H. J. 1986, A&AS, 65, 511

Mihalas, D., & Binney, J. 1981, Galactic Astronomy, W. H. Freeman and Cie, New York

Morrison, R., & McCammon, D. 1983, ApJ, 270, 119

Predehl, P., & Schmitt, J. H. M. M. 1995, A&A, 293, 889

Raymond, J. C., & Smith, B. W. 1977,ApJS, 35, 419

Saken, J. M., Fesen, R. A. , & Shull, J. M. 1992,ApJS, 81, 715

Sedov, L. I. 1959, Similarity and Dimensional Methods in Mechanics, (New York: Academic)

Shelton, R. A.,Cox, D. P., Maciejewski, W., Smith, R. K., Plewa, T., Pawl, A, and Rozyczka, M. 1999, ApJ, 524, 192

Slane, P. O., et al. 2000, in preparation.

Smith, R. & Cox, D. 2000, ApJ, submitted

Snowden, S. L., McCammon, D., Burrows, D. N., & Mendenhall, J. A. 1994, ApJ, 424, 714

Spitzer, L. Jr. 1956, Physics of Fully Ionized Gases, (New York: Interscience), p. 87

Taylor, G. I. 1950, Proc Royal Soc London, 201, 159

Thielemann, F.-K., Nomoto, K., & Hashimoto, M. 1996,ApJ, 460, 408

Turatto, M., Benetti, S., Cappellaro, E., Danziger, I. J., della Valle, M., Gouiffes, C., Mazzali, P. A., and Patat, F. 1996, MNRAS, 283 , 1

White, R. L., & Long, K. S. 1991, ApJ, 373, 543

Winkler, P. F., & Hanson, G. J. 1993, IAU Circ No. 5715

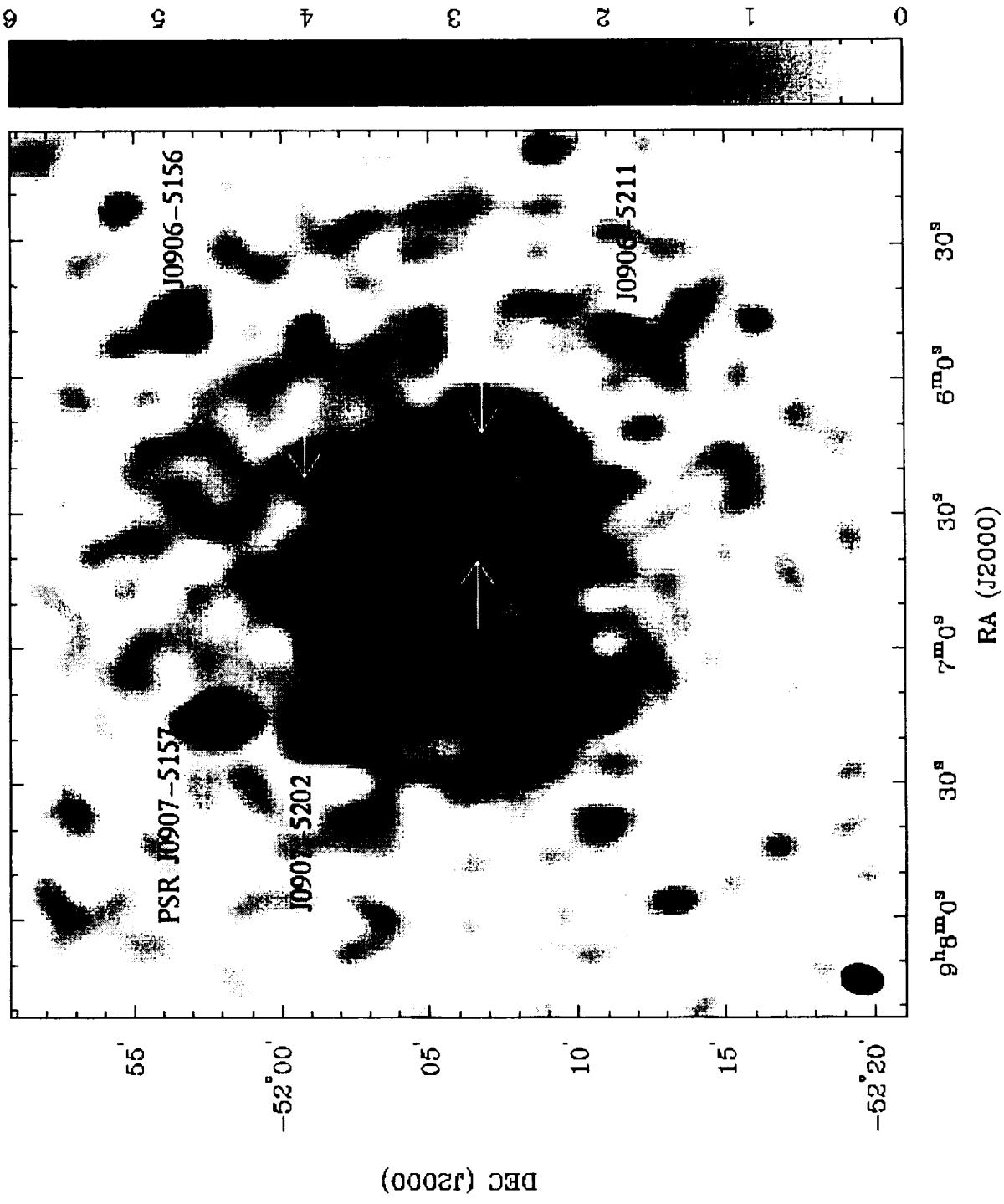

Fig. 1.— Radio image of G272.2−3.2 taken with the Australian Telescope Compact Array (ATCA) at 1.4 GHz. The optical filaments are indicated with by arrows. The positions of nearby pulsars are also indicated (Duncan et al. 1997).

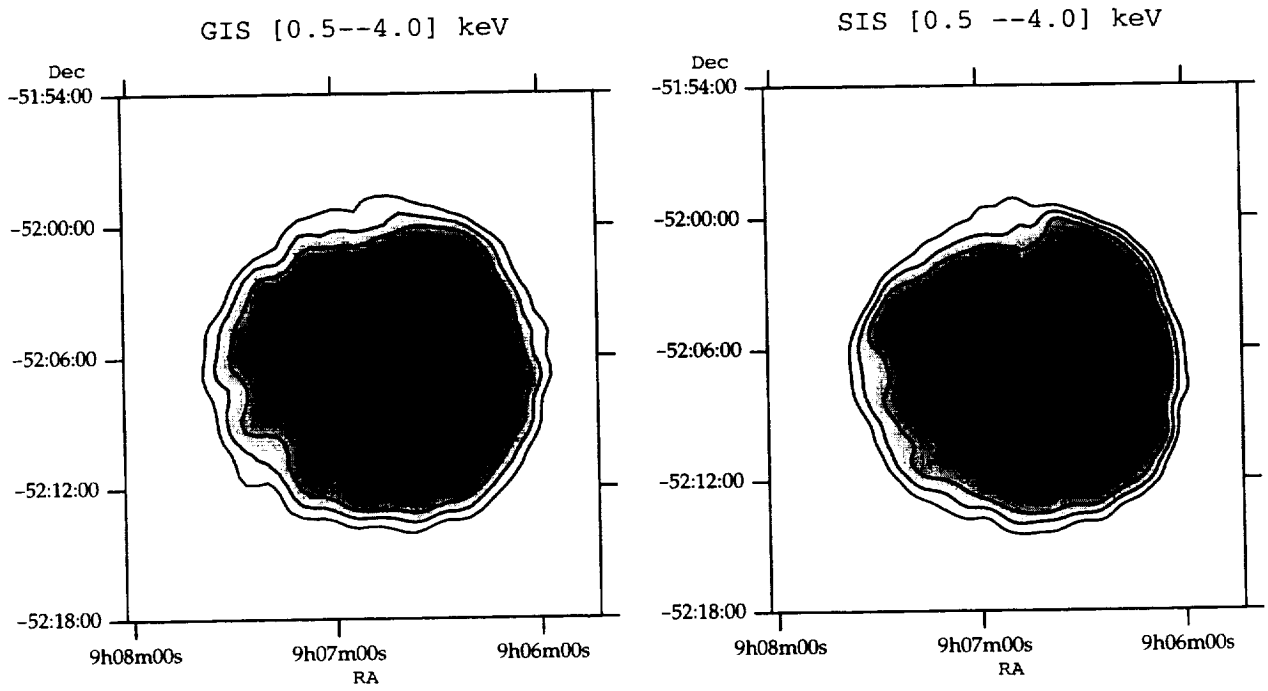

Fig. 2.— *ASCA* GIS(left) and SIS(right) images of G272.2−3.2 between 0.5 and 4.0 keV. Contour values are linearly spaced from 30% to 90% of the peak surface brightness in each map. Peak/Background values are (2.47/0.12) for the GIS and (3.20/0.19) for the SIS. All numbers are expressed in units of 10^{-3} counts s^{-1} $arcmin^{-2}$.

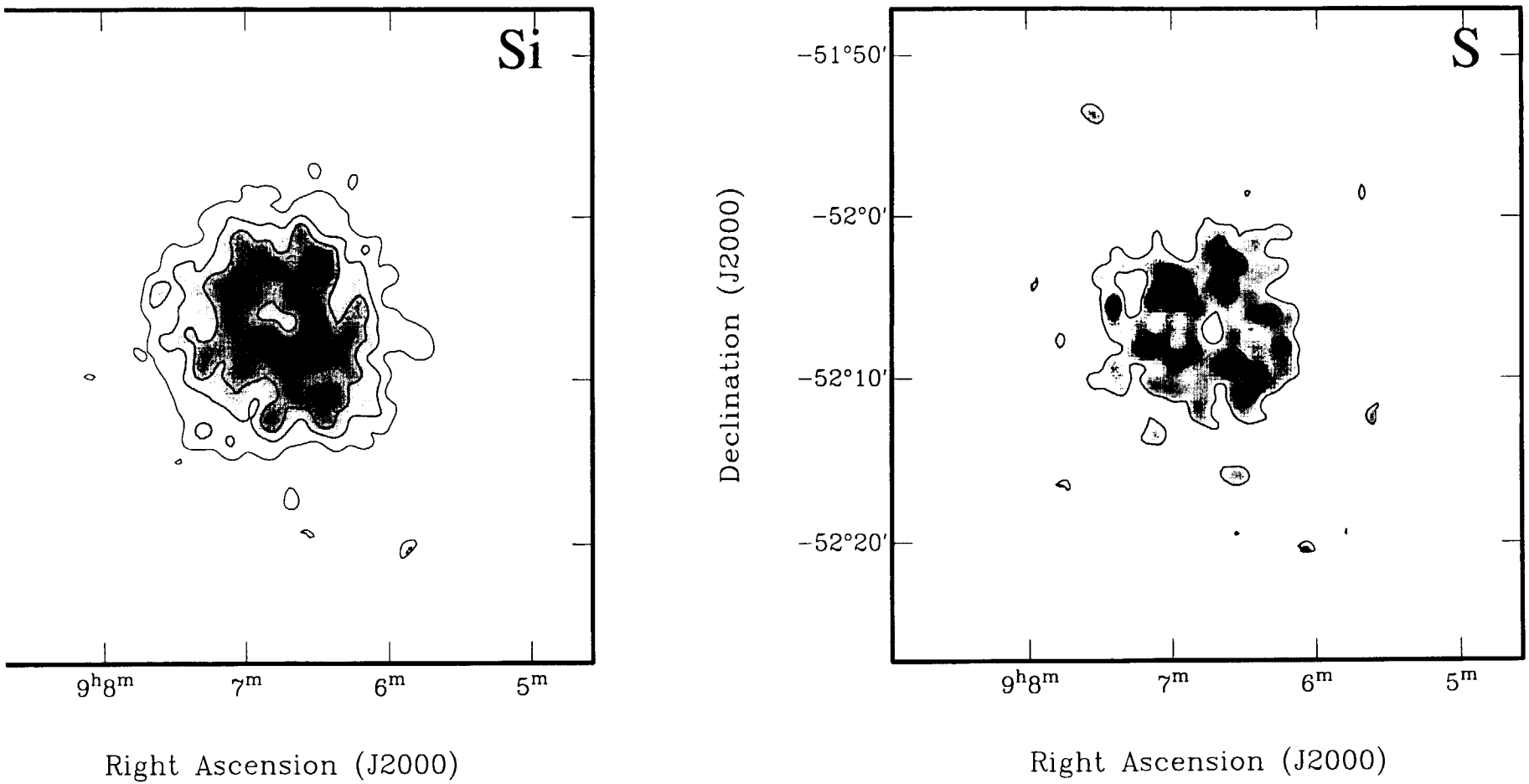
[1.70--1.90] keV
Si
[2.25--2.50] keV
S
−51°50′
−52°0′
−52°10′
−52°20′
Declination (J2000)
9h8m
7m
6m
5m
Right Ascension (J2000)
Right Ascension (J2000)

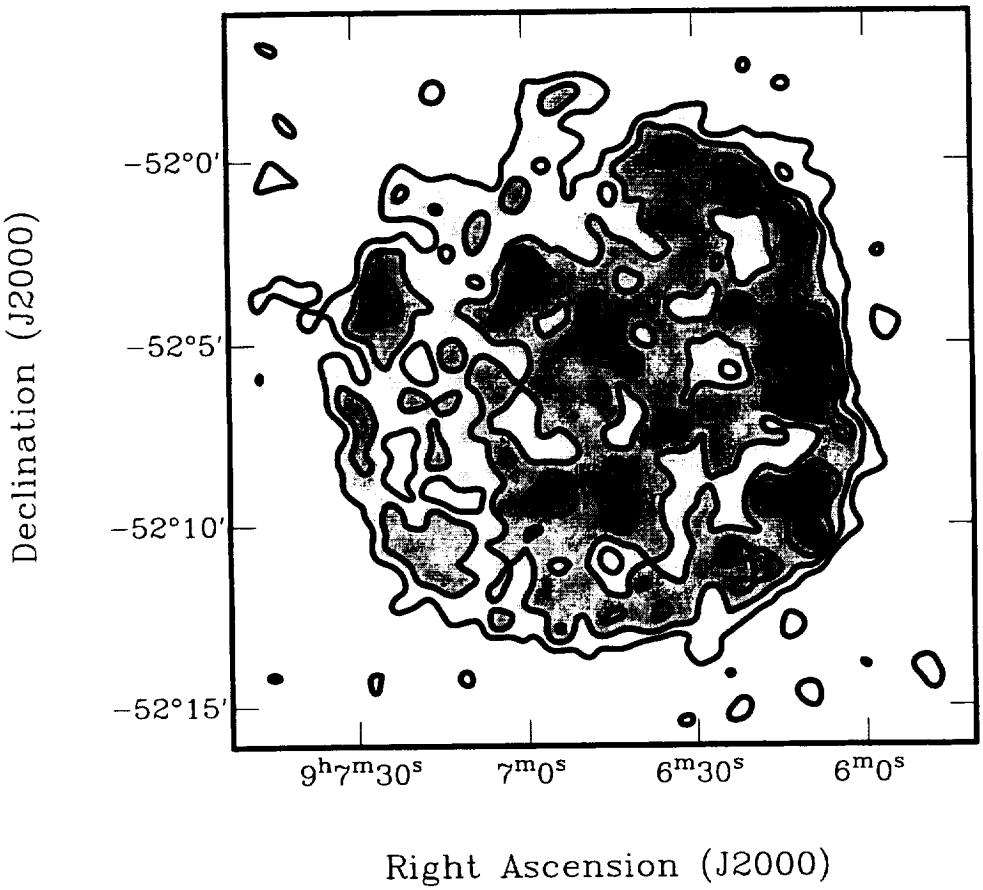

Fig. 4.— *ROSAT* HRI image of G272.2−3.2 after standard processing (Snowden et al. 1994).

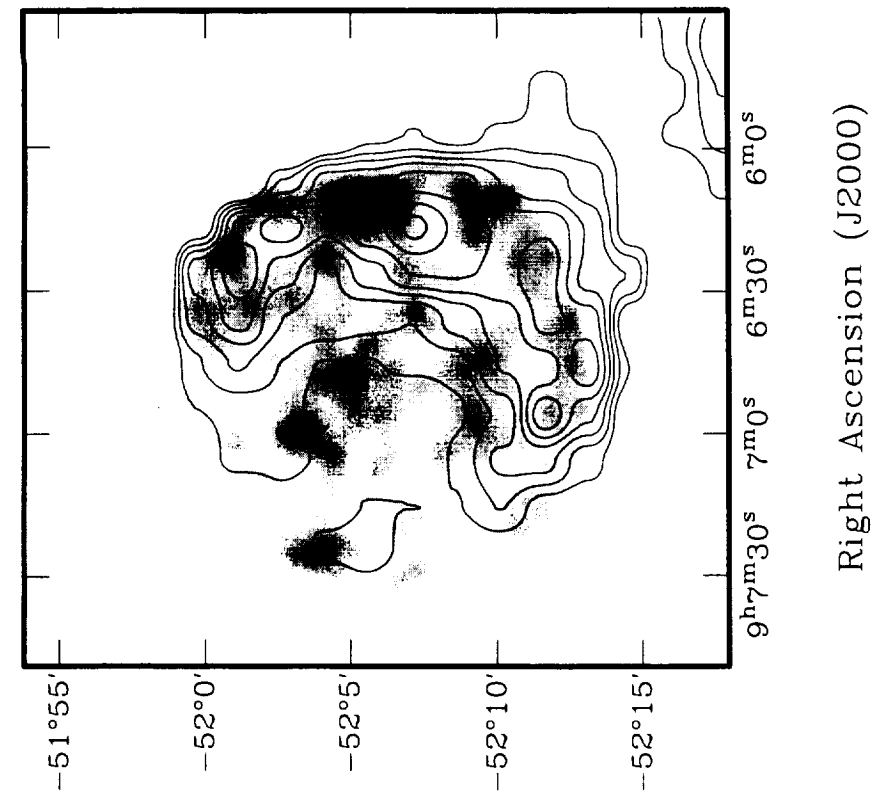
−51°55′
−52°0′
−52°5′
−52°10′
−52°15′
9h7m30s
7m0s
6m30s
6m0s
Declination (J2000)
Right Ascension (J2000)

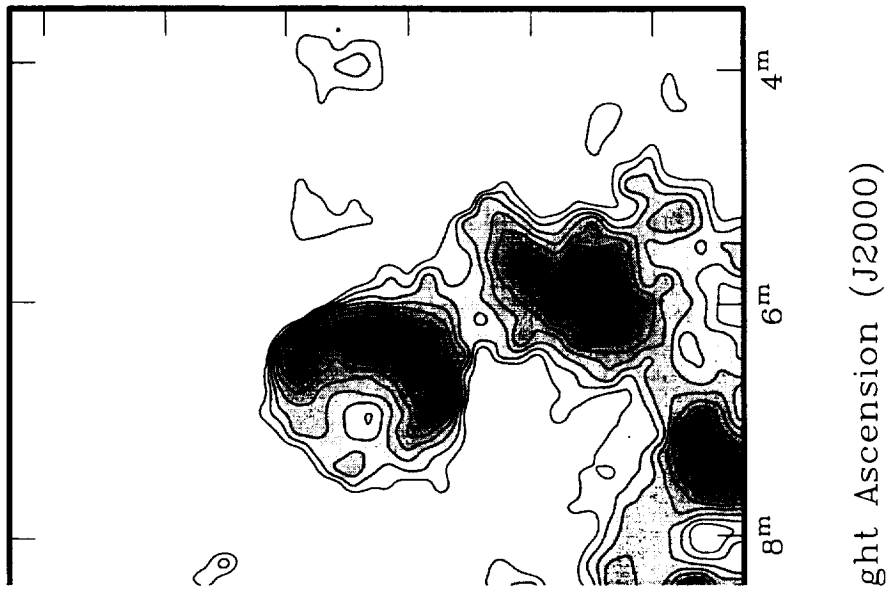
8m
6m
4m
ght Ascension (J2000)

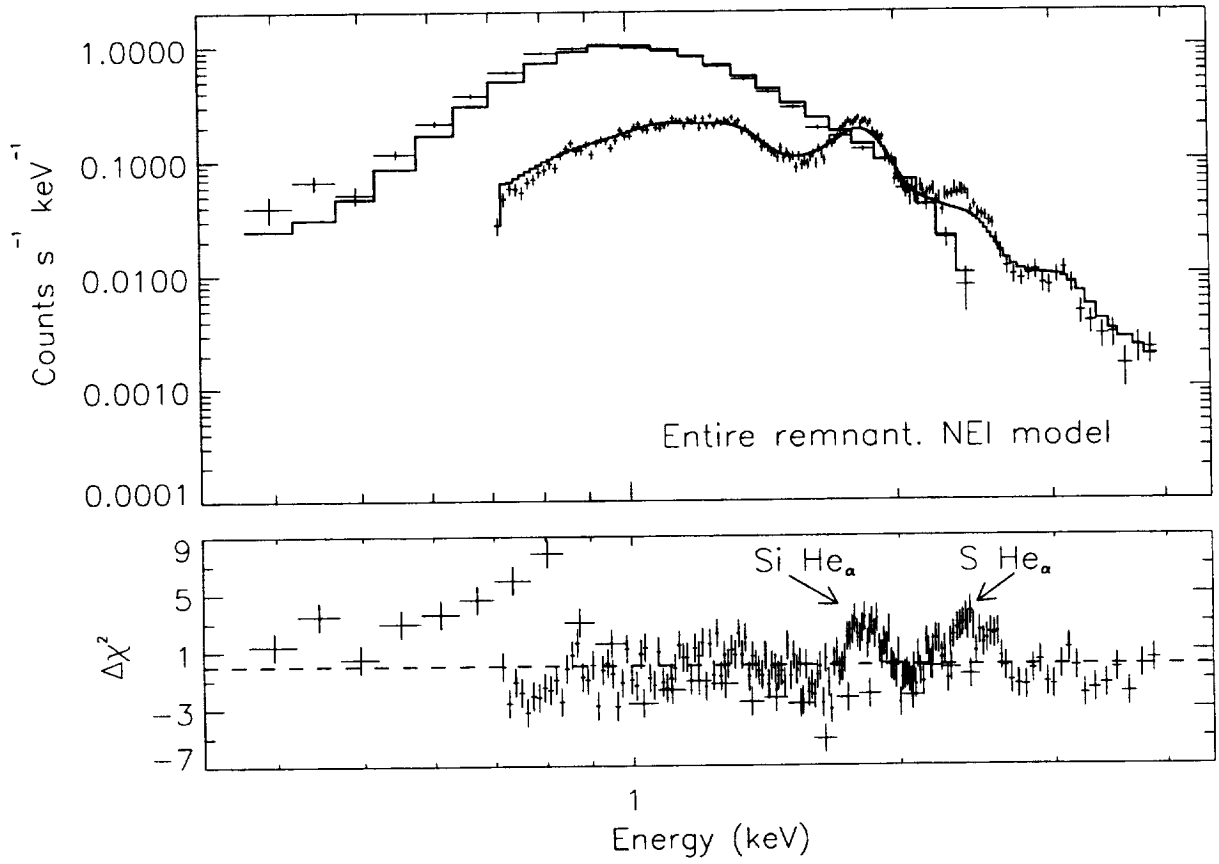

Fig. 6.— Spectra of the complete remnant for *ROSAT* PSPC and *ASCA* GIS. The two GIS detectors have been merged for display purposes only. The solid curves in the top panels show the best-fit NEI thermal plasma; the bottom panels plot the data/model residuals.

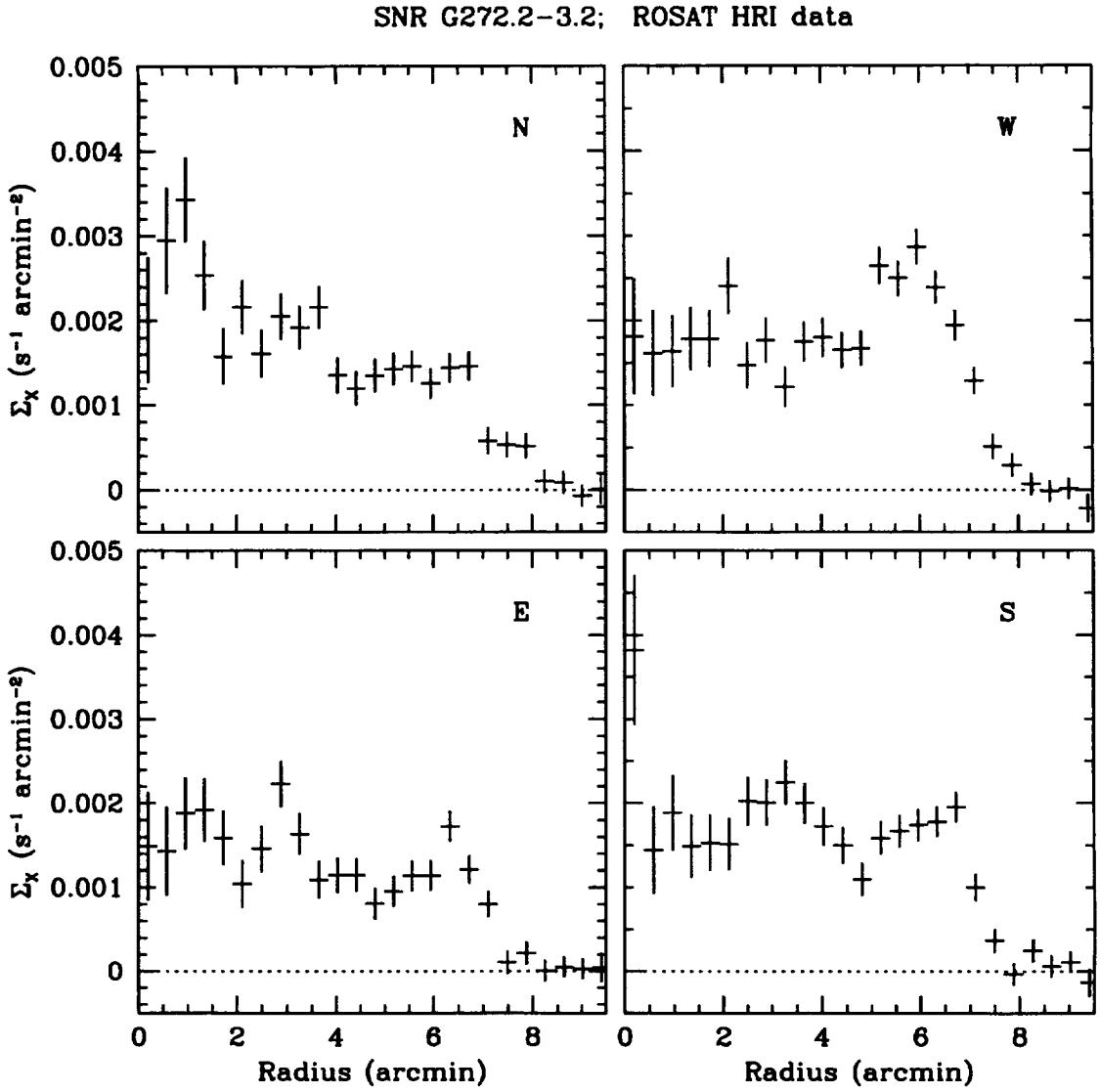

Fig. 7.— *ROSAT* HRI profile of the remnant extracted in 4 quadrants - We have chosen the cut so that region A , the region of bright optical filaments, fall into only one quadrant.

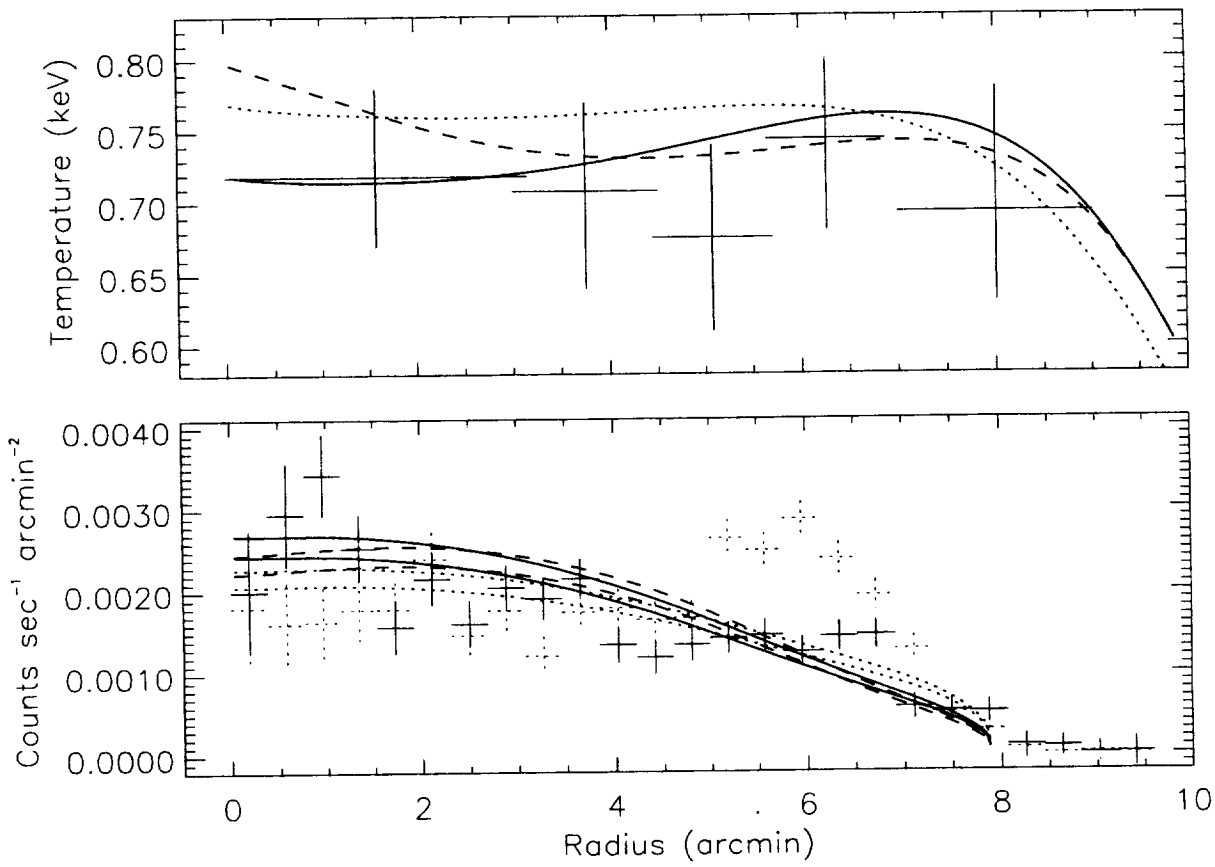

Fig. 8.— Radial temperature variation across the remnant (only up to the first five bins, representing the extent of the remnant) and the associated variation of the surface brightness. The temperature is measured using the *ASCA* GIS . The emission weighted temperature variation associated with the models is shown as well. The simulated profile is generated using *ROSAT* HRI. We have shown two extremes results: one obtained for the Northern quadrant (as defined in Fig. 7) shown in solid lines and one for the Western quadrant shown in dotted lines. We have shown the results from White & Long simulation using 3 different values of (C,τ). Results for (C,τ)=(100,33) are shown in solid lines. Dotted lines are for (C,τ)=(50,20) and dashed lines are for (C,τ)=(35,10). We have also indicated the range of normalization allowed by the error bars in the fit.

Table 1.
Results from the Spectral Analysis

Parameter	Fit results
Complete remnant (GIS and *ROSAT* PSPC), NEI thermal model[a]	
$N_{\rm H}$ (atoms cm^{-2})	$1.12\pm0.02\times10^{22}$
kT (keV)	$0.73^{+0.03}_{-0.04}$
$\log(n_e t)$ (cm^{-3} s)	$10.83^{+0.06}_{-0.08}$
Normalization(cm^{-5})[b]	$(3.5\text{–}3.8)\times10^{12}$
Flux (ergs cm^{-2} s^{-1}) ([0.2 – 3.0] keV)	$(2.2\text{–}2.5)\times10^{-10}$
Flux (ergs cm^{-2} s^{-1}) ([3.0 – 10.0] keV)	$(4.3\text{–}4.6)\times10^{-13}$
Flux (ergs cm^{-2} s^{-1}) ([0.4 – 2.4] keV)	$(2.0\text{–}2.3)\times10^{-10}$
χ^2/ν	691.95/354

[a] Single-parameter 1 σ errors
[b] N=$(\frac{n_{\rm H} n_e V}{4\pi D^2})$

Table 2a. Region A, NEI thermal model

Parameter	Fit results
$N_{\rm H}$ (atoms cm^{-2})	$1.17^{+0.02}_{-0.06}\times10^{22}$
kT (keV)	$0.86^{+0.08}_{-0.22}$
$\log(n_e t)$ (cm^{-3} s)	$10.38^{+0.32}_{-0.04}$
Normalization (cm^{-5})	$(1.35–3.50)\times10^{11}$
Flux (ergs cm^{-2} s^{-1}) ([0.2 - 3.0] keV)	$(1.6–4.1)\times10^{-11}$
Flux (ergs cm^{-2} s^{-1}) ([3.0 - 10.0] keV)	$(2.3–5.9)\times10^{-14}$
Flux (ergs cm^{-2} s^{-1}) ([0.4 - 2.4] keV)	$(1.4–3.6)\times10^{-11}$
χ^2/ν	248.35/133

Table 2b. Region A, NEI thermal model; Magnesium Abundance varies freely

Parameter	Fit results
$N_{\rm H}$ (atoms cm^{-2})	$0.95^{+0.07}_{-0.10}\times10^{22}$
kT (keV)	$1.00^{+0.35}_{-0.08}$
$\log(n_e t)$ (cm^{-3} s)	$10.64^{+0.37}_{-0.22}$
Normalization (cm^{-5})	$(0.6–1.9)\times10^{11}$
[Mg]/[Mg]$_\odot$ (*ROSAT*; SIS 0&1; GIS 2&3)	$0.5^{+0.8}_{-0.4}$;$2.2^{+2.8}_{-0.9}$; $2.7^{+3.5}_{-1.3}$; $1.4^{+1.7}_{-0.7}$; $1.2^{+1.6}_{-0.5}$
Flux (ergs cm^{-2} s^{-1}) ([0.2 - 3.0] keV)	$(0.5–1.5)\times10^{-11}$
Flux (ergs cm^{-2} s^{-1}) ([3.0 - 10.0] keV)	$(2.3–7.6)\times10^{-14}$
Flux (ergs cm^{-2} s^{-1}) ([0.4 - 2.4] keV)	$(0.46–1.43)\times10^{-11}$
χ^2/ν	176.1/129

Table 3. Region B, NEI thermal model

Parameter	Fit results
$N_{\rm H}$ (atoms cm^{-2})	$1.30^{+0.03}_{-0.04}\times10^{22}$
kT (keV)	$0.65^{+0.06}_{-0.02}$
$\log(n_e t)$ (cm^{-3} s)	$11.11^{+0.10}_{-0.15}$
Normalization (cm^{-5})	$(0.7\text{–}1.6)\times10^{12}$
Flux (ergs cm^{-2} s^{-1}) ([0.2 - 3.0] keV)	$(2.9\text{–}7.2)\times10^{-11}$
Flux (ergs cm^{-2} s^{-1}) ([3.0 - 10.0] keV)	$(0.7\text{–}1.6)\times10^{-13}$
Flux (ergs cm^{-2} s^{-1}) ([0.4 - 2.4] keV)	$(2.8\text{–}6.7)\times10^{-11}$
χ^2/ν	635/317